

A Comparison of Popular Point Configurations on \mathbb{S}^2

D.P. Hardin*, T. Michaels*[†] and E.B. Saff*

October 25, 2016

Abstract

There are many ways to generate a set of nodes on the sphere for use in a variety of problems in numerical analysis. We present a survey of quickly generated point sets on \mathbb{S}^2 , examine their equidistribution properties, separation, covering, and mesh ratio constants and present a new point set, equal area icosahedral points, with low mesh ratio. We analyze numerically the leading order asymptotics for the Riesz and logarithmic potential energy for these configurations with total points $N < 50,000$ and present some new conjectures.

Keywords. Spiral Nodes, Equal Area Nodes, Mesh Ratio, Riesz Energy, Low Discrepancy

2000 Mathematics Subject Classification. Primary: 52C35 Secondary: 65D15

*Center for Constructive Approximation, Department of Mathematics, Vanderbilt University, Nashville, TN 37240, USA, email: doug.hardin@vanderbilt.edu, timothy.j.michaels@vanderbilt.edu, and edward.b.saff@vanderbilt.edu The research of the authors was supported, in part, by US-NSF grants DMS-1412428 and DMS-1516400.

[†]The research of this author was completed as part of a Ph.D dissertation

1 Introduction

1.1 Overview

Distributing points on $\mathbb{S}^2 := \{x \in \mathbb{R}^3 : |x| = 1\}$ is a classical problem arising in many settings in numerical analysis and approximation theory, in particular the study of radial basis functions, quadrature and polynomial interpolation, Quasi-Monte Carlo methods for graphics applications, finite element methods for PDE's, cosmic microwave background radiation modeling, crystallography and viral morphology, to name a few. The goal of this paper is to survey some widely used algorithms for the generation of spherical node sets. We will restrict our descriptions to “popular” point sets, most of which can be generated “reasonably fast.” Namely, we study

- Fibonacci and generalized spiral nodes
- projections of low discrepancy nodes from the unit square
- zonal equal area nodes and HEALPix nodes
- polygonal nodes such as icosahedral, cubed sphere, and octahedral nodes
- minimal energy nodes
- maximal determinant nodes
- random nodes and
- “mesh icosahedral equal area nodes.”

The last is a new point set devised to have many desirable properties. For each of the above configurations, we provide illustrations, and analyze several of their properties. We focus our attention primarily on

- equidistribution
- separation
- covering
- quasi-uniformity and
- Riesz potential energy.

For each property we provide numerical calculations, tables, and comparisons, and in some cases we prove theoretical bounds on the mesh ratio. Section 3 is devoted to asymptotic comparisons of various potential energies. We do not consider quadrature of the point sets; however, such a comparison for several of the configurations we describe here can be found in [19]. We now formally introduce the properties we will be studying and, in Section 2, describe the point sets themselves. We leave the technical proofs to Section 4, and at the end of the document, we provide resources for Matlab source codes to generate the point sets.

1.2 Definitions and Properties

For low error numerical integration with respect to uniform surface area measure ([1] and [35]) as well as in digitizing \mathbb{S}^2 for computer graphics purposes ([39] and [40]), it is important for any spherical configuration to have an approximately uniform distribution. A sequence $\{\omega_N\}_{N=1}^\infty$ of spherical point sets with ω_N having cardinality N is called *equidistributed* if the sequence of normalized counting measures,

$$\nu_N(A) := \frac{1}{N} |A \cap \omega_N|, \quad A \text{ Borel set,}$$

associated with the ω_N 's converges in the weak-star sense to σ , the normalized surface area measure on \mathbb{S}^2 , as $N \rightarrow \infty$. That is, for all continuous functions f on \mathbb{S}^2 ,

$$\lim_{N \rightarrow \infty} \int_{\mathbb{S}^2} f d\nu_N = \int_{\mathbb{S}^2} f d\sigma.$$

An equivalent definition is that the L_∞ -spherical cap discrepancy

$$D_C(\omega_N) := \sup_{V \subset \mathbb{S}^2} \left| \frac{|V \cap \omega_N|}{N} - \sigma(V) \right| \rightarrow 0, \quad N \rightarrow \infty,$$

where the supremum is taken over all spherical caps $V \subset \mathbb{S}^2$.

For the study of local statistics, separation and covering properties play an important role. The *separation* of a configuration $\omega_N \subset \mathbb{S}^2$ is

$$\delta(\omega_N) := \min_{\substack{x, y \in \omega_N \\ x \neq y}} |x - y|,$$

and a sequence of spherical N -point configurations is said to be *well-separated* if for some $c > 0$ and all $N \geq 2$,

$$\delta(\omega_N) \geq cN^{-1/2}.$$

The *covering radius* of ω_N with respect to \mathbb{S}^2 is defined to be

$$\eta(\omega_N) := \max_{y \in \mathbb{S}^2} \min_{x \in \omega_N} |x - y|,$$

and a sequence of spherical N -point configurations is a *good-covering* if for some $C > 0$ and all $N \geq 2$,

$$\eta(\omega_N) \leq CN^{-1/2}.$$

A sequence of configurations $\{\omega_N\}_{N=2}^\infty$ is said to be *quasi-uniform* if the sequence

$$\left\{ \gamma(\omega_N) := \frac{\eta(\omega_N)}{\delta(\omega_N)} \right\}_{N \geq 2}$$

is bounded as $N \rightarrow \infty$. The quantity $\gamma(\omega_N)$ is called the *mesh ratio* of ω_N . Note that some authors define the mesh ratio as $2\gamma(\omega_N)$. A sequence of N -point configurations is quasi-uniform if it is well-separated and a good-covering. We remark that equidistribution does not imply quasi-uniformity or vice versa. In applications involving radial basis functions, “1-bit” sensing, and finite element methods ([27], [41], [50], and [58]), there is interest in precise bounds on

$D_C(\omega_N)$, $\delta(\omega_N)$, $\eta(\omega_N)$, and $\gamma(\omega_N)$. A trivial lower bound is $\gamma(\omega_N) \geq 1/2$ for any configuration. Asymptotically, as proved in [9],

$$\gamma(\omega_N) \geq \frac{1}{2 \cos \pi/5} + o(1) = \frac{\sqrt{5}-1}{2} + o(1), \quad N \rightarrow \infty,$$

for any sequence of configurations $\{\omega_N\}_{N=2}^\infty \subset \mathbb{S}^2$.

We also evaluate the potential energy of our point sets. The problem of minimizing point energies on the sphere dates to at least the beginning of the 20th century when Thomson put forth a model of the ground state configurations of electrons in [62]. Given a lower-semicontinuous, symmetric kernel $K : \mathbb{S}^2 \times \mathbb{S}^2 \rightarrow (-\infty, \infty]$, and a spherical configuration $\omega_N \subset \mathbb{S}^2$, the K -energy of ω_N is defined to be

$$E_K(\omega_N) := \sum_{\substack{x, y \in \omega_N \\ x \neq y}} K(x, y). \quad (1)$$

The infimum of $E_K(\omega_N)$ over all N -point configurations on \mathbb{S}^2 is attained and is denoted by $\mathcal{E}_K(N)$. We will restrict our attention to the class of Riesz kernels defined by

$$\begin{aligned} K_s(x, y) &= \frac{1}{|x - y|^s}, & s > 0 \\ K_{\log}(x, y) &= \log \frac{1}{|x - y|}, \\ K_s(x, y) &= -|x - y|^{-s}, & s < 0. \end{aligned}$$

For brevity, the energy and minimal energy quantities for the Riesz s -kernel and log kernel will be denoted by $E_s(\omega_N)$, $E_{\log}(\omega_N)$, $\mathcal{E}_s(N)$, and $\mathcal{E}_{\log}(N)$ respectively. Determining an exact minimal configuration for a fixed N and s is a highly non-linear optimization problem. In practice, gradient descent and Newton methods are used to arrive at approximate global minima [20]; however, there is substantial interest in generating nearly optimal points more quickly [53].

The *Voronoi cell* of a point $x \in \omega_N \subset \mathbb{S}^2$ is the spherical polygon

$$V_x(\omega_N) := \{y \in \mathbb{S}^2 : |y - x| \leq |y - z|, \forall z \in \omega_N \setminus \{x\}\}.$$

The *Voronoi decomposition* of a configuration is

$$V(\omega_N) := \{V_x(\omega_N)\}_{x \in \omega_N}.$$

It has been observed that the Voronoi cell decomposition of nearly optimal energy configurations appears to consist primarily of nearly regular spherical hexagons mixed with “scars” of spherical heptagons and pentagons as shown in Figure 1. It has been conjectured that for $s > 2$, the dominant term in the asymptotic expansion of $\mathcal{E}_s(N)$ is related to the Epstein-Zeta function for the hexagonal lattice (see Section 3).

We conclude this section by introducing some secondary properties of spherical configurations that we will use: A partition $P_N := \{W_i\}_{i=1}^N$ of \mathbb{S}^2 into N cells whose pairwise intersections have σ -measure 0 is *equal area* if $\sigma(W_i) = 1/N$ for all $1 \leq i \leq N$. A sequence of partitions $\{P_N\}_{N=2}^\infty$ of \mathbb{S}^2 such that each P_N

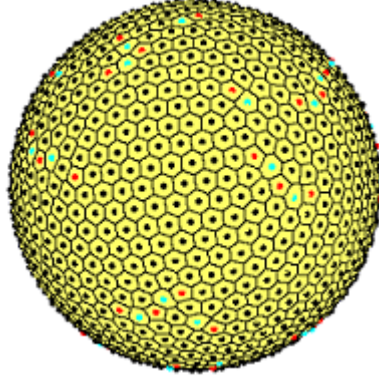


Figure 1: Voronoi decomposition of approximately minimal energy nodes for $N = 1000$ and $s = 2$. Cells with black points are hexagonal, but not necessarily regular. Cells with red points are pentagonal and cells with cyan points are heptagonal (see online for color).

has N cells is *diameter bounded* if there are constants $c, C > 0$ such that for all $N \in \mathbb{N}$ and for every cell $W_i^N \in P_N$,

$$cN^{-1/2} \leq \text{diam } W_i^N \leq CN^{-1/2}, \quad (2)$$

where $\text{diam}(A) := \sup_{x,y \in A} |x - y|$. We will call a sequence of partitions of \mathbb{S}^2 *asymptotically equal area* if

$$\lim_{N \rightarrow \infty} N \max_{1 \leq i \leq N} \sigma(W_i^N) = \lim_{N \rightarrow \infty} N \min_{1 \leq i \leq N} \sigma(W_i^N) = 1, \quad (3)$$

and a sequence of spherical configurations $\{\omega_N\}_{N=1}^\infty$ will be said to be asymptotically equal area if its sequence of Voronoi decompositions is asymptotically equal area.

2 Point Sets on \mathbb{S}^2

Generalized Spiral Points

A spherical spiral on \mathbb{S}^2 is a path in spherical coordinates of the form

$$r = 1, \quad \theta = L\phi, \quad 0 \leq \phi \leq \pi,$$

where ϕ denotes the polar angle and θ the azimuth. Modifying a construction by Rakhmanov, Saff, and Zhou [47], Bauer [2] defines a sequence of N points lying on a generating spherical spiral, S_N :

$$L = \sqrt{N\pi}, \quad h_k = 1 - \frac{2k-1}{N}, \quad \phi_k = \cos^{-1}(h_k), \quad \theta_k = L\phi_k, \quad k = 1, \dots, N. \quad (4)$$

The slope L is chosen such that for large N , the distance between adjacent points on the same level of the curve is similar to the distance between adjacent levels which differ by 2π in θ . Indeed, the geodesic spacing between turns of the spiral is given by $2\pi/L = \sqrt{4\pi/N}$. Meanwhile, the total arc length is

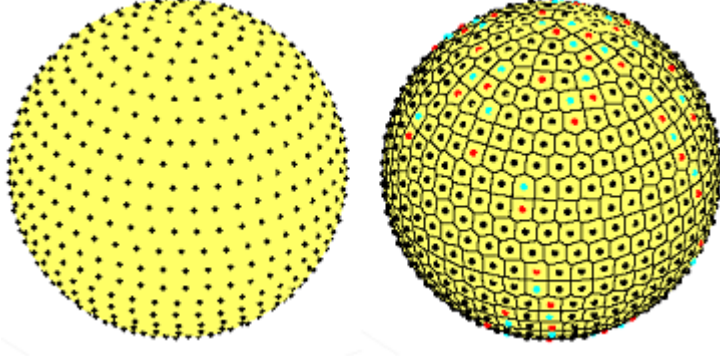


Figure 2: Plot of $N = 700$ generalized spiral points and their Voronoi decomposition.

$$T = \int_{S_N} \sqrt{d\phi^2 + d\theta^2 \sin^2 \phi} = \int_0^\pi \sqrt{1 + L^2 \sin^2 \phi} d\phi = 2\sqrt{1 + L^2} E(L/\sqrt{1 + L^2}),$$

where $E(\cdot)$ is the complete elliptic integral of the second kind. For large N , $T \approx 2L$, and the spiral is divided into nearly equal length segments of approximately $2L/N = \sqrt{4\pi/N}$. We refer to these points as the *generalized spiral points*.

Theorem 1. *The sequence $\{\omega_N\}_{N=1}^\infty$ of generalized spiral point configurations is equidistributed on \mathbb{S}^2 , quasi-uniform, and has the following asymptotic separation property:*

$$\lim_{N \rightarrow \infty} \sqrt{N} \delta(\omega_N) = \sqrt{8 - 4\sqrt{3} \cos(\sqrt{2\pi}(1 - \sqrt{3}))} \approx 3.131948... \quad (5)$$

As shown in the proof of Theorem 1, the Voronoi cells of ω_n are asymptotically equal area, but do not approach regular hexagons. Indeed, a typical decomposition is shown in Figure 2. A comparison of the mesh ratios for several values of N is shown in Table 1. Numerically, the mesh ratio appears to converge to 0.8099....

Table 1: Mesh Ratios for Generalized Spiral Nodes

N	$\gamma(\omega_N)$	N	$\gamma(\omega_N)$	N	$\gamma(\omega_N)$
10	0.897131	400	0.816007	20000	0.809510
20	0.827821	500	0.810128	30000	0.809629
30	0.814383	1000	0.805465	40000	0.809689
40	0.826281	2000	0.806411	50000	0.809725
50	0.834799	3000	0.807510	100000	0.809797
100	0.803901	4000	0.808077	200000	0.809832
200	0.806020	5000	0.808435	300000	0.809844
300	0.809226	10000	0.809151	500000	0.809854

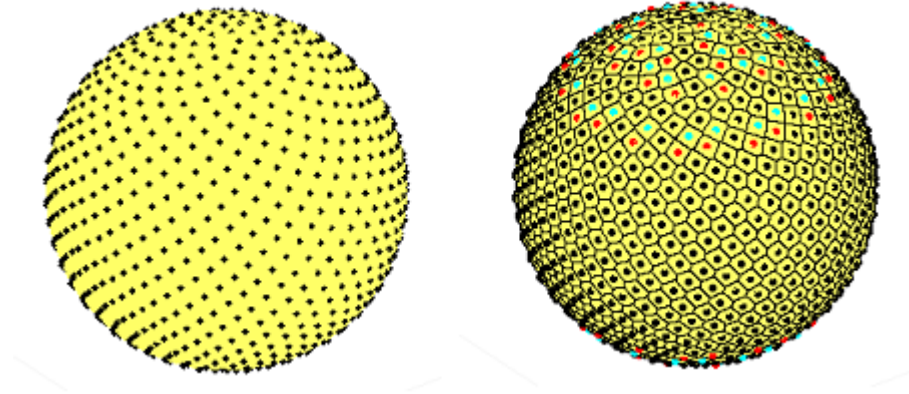


Figure 3: Fibonacci nodes for $N = 1001$ as defined by Swinbank and Purser and corresponding Voronoi decomposition. The visible spirals at each level are generated by a sequence of points whose index increases arithmetically by a Fibonacci number.

Fibonacci Nodes

Another set of spiral points is modeled after nodes appearing in nature such as the seed distribution on the head of a sunflower or a pine cone, a phenomenon known as spiral phyllotaxis [25]. Coxeter [22] demonstrated these arrangements are fundamentally related to the Fibonacci sequence, $\{F_k\} = \{1, 1, 2, 3, 5, 8, 13, \dots\}$ and the golden ratio $\varphi = (1 + \sqrt{5})/2$. There are two similar definitions of the spherical point set in the literature. Both are defined as lattices on the square $[0, 1)^2$ and then mapped to the sphere by the Lambert cylindrical equal area projection, denoted by Λ . In Cartesian coordinates, Λ is defined by

$$\Lambda(x, y) := (\sqrt{1 - (2y - 1)^2} \cos 2\pi x, \sqrt{1 - (2y - 1)^2} \sin 2\pi x, 2y - 1)$$

and, in spherical coordinates, by

$$\Lambda(x, y) := (\cos^{-1}(2y - 1), 2\pi x) = (\phi, \theta).$$

Define a rational lattice on $[0, 1)^2$, with total points F_k by

$$\tilde{\omega}_{F_k} := \left(\left\{ \frac{iF_{k-1}}{F_k} \right\}, \frac{i}{F_k} \right), \quad 0 \leq i \leq F_k, \quad (6)$$

where $\{x\} = x - \lfloor x \rfloor$ denotes the fractional part of x . On the other hand, an irrational lattice can be formed similarly for all values of total points N by replacing F_{k-1}/F_k in (6) by $\lim_{k \rightarrow \infty} F_{k-1}/F_k = \varphi^{-1}$:

$$\tilde{\omega}_N := \left(\{i\varphi^{-1}\}, \frac{i}{N} \right), \quad 0 \leq i \leq N.$$

Swinbank and Purser [59] define a spherical point set for all odd integers $2N + 1$ symmetrically across the equator derived from the irrational lattice with points shifted a half step away from the poles:

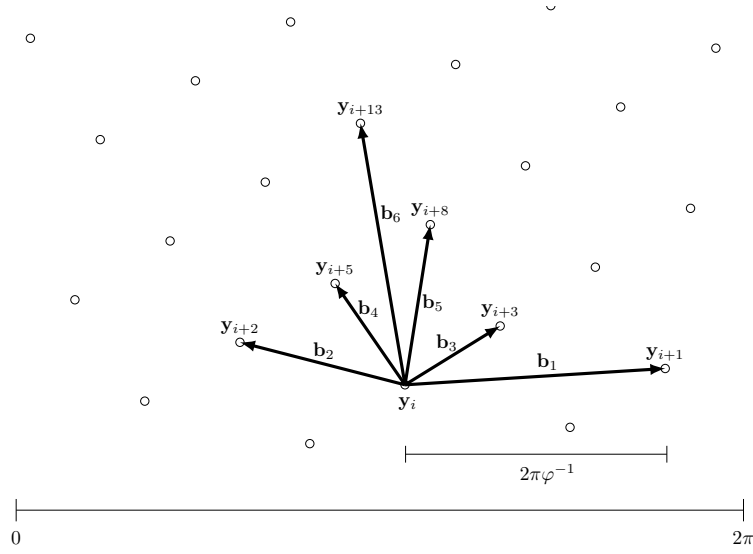


Figure 4: Irrational lattice points on the square with labeled basis vectors from [59] around a node \mathbf{y}_i . The configuration is approximately a rotation of the rectangular lattice by the angle $\tan^{-1}(\varphi)$. Each line of points along a basis vector is mapped to a spiral under the Lambert projection, Λ . The basis vector \mathbf{b}_k such that $\Lambda(\mathbf{b}_k)$ has the shortest length forms the visible dominant spirals emanating from $\Lambda(\mathbf{y}_i)$. These shortest length vectors are determined by the total number of points and zone number z .

$$\theta_i = 2\pi i\varphi^{-1}, \quad \sin \phi_i = \frac{2i}{2N+1}, \quad -N \leq i \leq N, \quad -\pi/2 \leq \phi_i \leq \pi/2.$$

Denote ω_{2N+1} as the configuration generated above. Whereas for large N , the generalized spiral points tend towards flattening out and partitioning the sphere into distinct regions of latitude, the Fibonacci points maintain visible clockwise and counterclockwise spirals as N grows. Labeling the points of ω_{2N+1} by increasing latitude, the dominant spirals emanating from $x_i \in \omega_{2N+1}$ are formed by the sequence $\{x_{i+jF_k}\}$ for some Fibonacci number F_k and $j = \dots, -2, -1, 0, 1, 2, \dots$.

The Fibonacci points derived from the rational lattice are studied by Aistleitner et al [1] and Bilyk et al [7] for discrepancy estimates. In [1], the spherical cap discrepancy of the points $\{F_k\}$ is bounded by

$$D_C(\Lambda(\tilde{\omega}_{F_k})) \leq \begin{cases} 44\sqrt{(2/F_k)} & \text{if } k \text{ is odd,} \\ 44\sqrt{(8/F_k)} & \text{if } k \text{ is even.} \end{cases}$$

Numerical experiments in [1] suggest that in fact,

$$D_C(\Lambda(\tilde{\omega}_{F_k})) = O\left(\frac{(\log F_k)^c}{F_k^{3/4}}\right), \quad k \rightarrow \infty \quad \text{for some } 1/2 \leq c \leq 1.$$

which is optimal up to a log power [3]. Both sequences of Fibonacci configurations are equidistributed. However, since the Swinbank and Purser nodes are

defined for more values of total points, we will take these to be the Fibonacci sets moving forward. In [59], these points are also numerically shown to be asymptotically equal area.

Analyzing ω_{2N+1} as a shifted irrational lattice mapped by the Lambert projection helps to visualize the underlying spiral structure. Define a system of basis vectors

$$\mathbf{b}_k = \Lambda^{-1}(x_{i+F_k}) - \Lambda^{-1}(x_i), \quad k = 1, 2, 3, \dots,$$

which are independent of base point x_i . This is illustrated in Figure 4. Emanating from each point x_i , the line of points $\{x_i + m\mathbf{b}_k\}_{m=\dots, -1, 0, 1, \dots}$ is mapped to a spiral on \mathbb{S}^2 under the Lambert projection. Like the Fibonacci sequence, the basis vectors satisfy

$$\mathbf{b}_{k+1} = \mathbf{b}_k + \mathbf{b}_{k-1}.$$

On the sphere, the basis vectors in terms of the local Cartesian coordinate system at a point $(\phi_i, \theta_i) \in \omega_{2N+1}$ have the form

$$\mathbf{c}_{k,i} = \left((-1)^k 2\pi \cos \phi_i \varphi^{-k}, \frac{2F_k}{(2N+1) \cos \phi_i} \right). \quad (7)$$

For a fixed latitude ϕ and total number of points $2N+1$, the zone number z is defined by

$$\varphi^{2z} = (2N+1)\pi\sqrt{5}\cos^2\phi.$$

Letting $d = \sqrt{4\pi/(\sqrt{5}(2N+1))}$ and using the fact that for large k , $F_k \approx \varphi^k/\sqrt{5}$ equation (7) can be rewritten

$$\mathbf{c}_{k,i} \approx d((-1)^k \varphi^{z-k}, \varphi^{k-z}). \quad (8)$$

For latitudes where $k-1/2 \leq z \leq k+1/2$, $\mathbf{c}_{k,i}$ has the minimum length of the basis vectors around x_i and forms the dominant spiral at those latitudes. As shown in [59], $|\mathbf{c}_{k,i}|$ is also the smallest distance between points near these latitudes. Thus, the Delaunay triangulation [46] of ω_{2N+1} is composed of $\mathbf{c}_{k,i}$, $\mathbf{c}_{k-1,i}$, and $\mathbf{c}_{k+1,i}$ when $k-1/2 \leq z \leq k+1/2$. This is shown in Figure 5 and allows us to prove quasi-uniformity.

Proposition 2. *The sequence of Fibonacci configurations is quasi-uniform.*

Numerically, the minimal separation appears to occur at the pole with value $|x_1 - x_4| = |x_{2N+1} - x_{2N-2}|$ and the largest hole appears to occur in the triangles covering the poles, $\triangle x_2, x_3, x_5$ and $\triangle x_{2N}, x_{2N-1}, x_{2N-3}$. In a straightforward computation, it can be shown that

$$\lim_{N \rightarrow \infty} \sqrt{2N+1} |x_1 - x_4| = \sqrt{16 - \sqrt{112} \cos(6\pi\varphi^{-1})} = 3.09207\dots$$

and the circumradius r of the polar triangles satisfies

$$\lim_{N \rightarrow \infty} \sqrt{2N+1} r = 2.72812\dots$$

As shown in Table 2, the mesh ratios for Fibonacci nodes appear to converge quickly to this ratio ≈ 0.882298 .

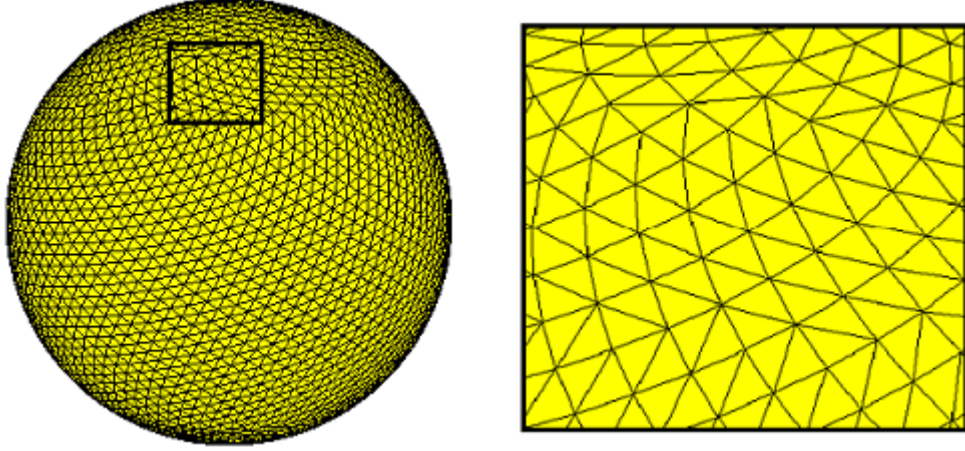


Figure 5: Triangulation of $N = 3001$ nodes viewed at a slightly different angle. The enlarged box demonstrates where zone number z changes with changing ϕ . The sudden shift occurs at $z = k \pm 1/2$. Along this latitude, $\mathbf{c}_{k,i}$ and $\mathbf{c}_{k\pm 1,i}$ have equal lengths. For $k - 1/2 < z < k + 1/2$, the triangulation consists of basis vectors $\mathbf{c}_{k,i}$ and $\mathbf{c}_{k+1,i}$ as proven in [59].

Table 2: Mesh Ratios for Fibonacci Nodes

N	$\gamma(\omega_N)$	N	$\gamma(\omega_N)$	N	$\gamma(\omega_N)$
11	0.859197	401	0.881897	20001	0.882289
21	0.872632	501	0.881978	30001	0.882292
31	0.876251	1001	0.882139	40001	0.882293
41	0.877909	2001	0.882218	50001	0.882294
51	0.878857	3001	0.882244	100001	0.882296
101	0.880646	4001	0.882258	200001	0.882297
201	0.881489	5001	0.882266	300001	0.882297
301	0.881762	10001	0.882282	500001	0.882297

Low Discrepancy Nodes

Another approach for distributing points on the sphere is to minimize a suitable notion of discrepancy, such as spherical cap, L_p , or generalized discrepancy (cf. [16] and [23]). A low spherical cap discrepancy sequence $\{\omega_N\}_{N=2}^{\infty}$ satisfies [3]

$$\frac{a}{N^{3/4}} \leq D_C(\omega_N) \leq A \frac{\sqrt{\log N}}{N^{3/4}}, \quad N \geq 2, \quad (9)$$

for some $a, A > 0$. Low discrepancy point sets are used in Quasi-Monte Carlo methods for numerical integration and also in graphics applications in [65]. One method for generating spherical nodes is to first distribute points on the square $[0, 1)^2$ with low planar discrepancy [45], i.e. for some $A > 0$

$$D(\omega_N) := \sup_R \left| \frac{R \cap \omega_N}{N} - \sigma(R) \right| \leq A \frac{\log N}{N}, \quad \omega_N \subset [0, 1)^2, \quad (10)$$

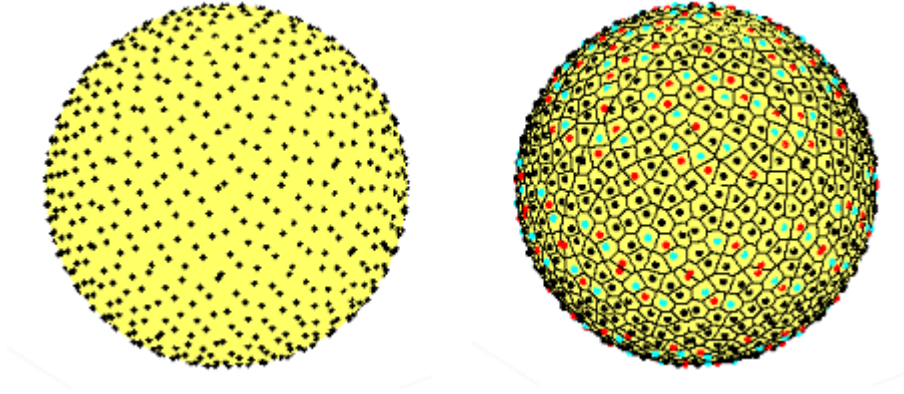


Figure 6: Hammersley nodes for $N = 1000$ and corresponding Voronoi decomposition.

where the supremum R is taken over all rectangles with sides parallel to the axes. These sequences are then mapped to the sphere via the Lambert projection. While the $\log N/N$ term in (10) is optimal on the plane [51], it is an open problem whether the images of these sequences have optimal order spherical cap discrepancy. There are several such node distributions in the literature (cf. [1] and [23]), but as their properties are similar, we only consider the following one.

Hammersley Nodes

For an integer $p \geq 2$, the p -adic van der Corput sequence is defined by

$$x_k^{(p)} = \frac{a_0}{p} + \cdots + \frac{a_r}{p^{r+1}}, \quad \text{where} \quad k = a_0 + \cdots + a_r p^r, \quad a_i \in \{0, 1\}.$$

The Hammersley node set on the square ([23], [45], and [65]) is given by $x_k := x_k^{(2)}$ and $y_k := \frac{2k-1}{2N}$. The N point spherical Hammersley node set is given by $\{\Lambda(2\pi x_k, 1 - 2y_k)\}_{k=1}^N$. The configuration for $N = 1000$ is given in Figure 6. The discrepancy of the planar Hammersley nodes is known from Niederreiter [45] to satisfy (10). The sequence of Hammersley configurations is equidistributed; however it is not well-separated or quasi-uniform. This makes the nodes poor candidates for energy, as shown in Section 3. Their Voronoi decompositions also exhibit no discernible geometric patterns.

Equal Area Partitions

Another class of point sets are those derived from equal area partitions of the sphere.

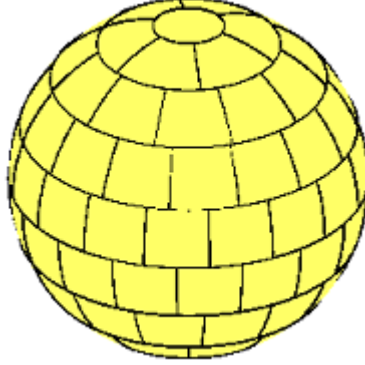


Figure 7: Zonal equal area partition of the sphere into 100 cells. The algorithm does not determine a unique partition as the collars can rotate past each other. Image created with the help of Paul Leopardi’s equal area partitioning toolbox available at eqsp.sourceforge.net.

Zonal Equal Area Nodes:

Rakhmanov et al [47] construct a diameter bounded, equal area partition of \mathbb{S}^2 into rectilinear cells of the form

$$R([\tau_\phi, \nu_\phi] \times [\tau_\theta, \nu_\theta]) := \{(\phi, \theta) \in \mathbb{S}^2 : \tau_\phi \leq \phi \leq \nu_\phi, \tau_\theta \leq \theta \leq \nu_\theta\}.$$

The cells are grouped by regions of equal latitude called collars that have the form $R([\tau_\phi, \nu_\phi] \times [0, 2\pi])$. The cells are defined such that $\nu_\phi - \tau_\phi$ and $\nu_\theta - \tau_\theta$ approximate $\sqrt{4\pi/N}$ as N grows. This ensures the correct order of the diameter bound. The cells are defined in the following way.

1. *Determine the latitudes of the polar caps.* The first two cells are taken to be the polar caps of radius $\phi_c = \cos^{-1}(1 - 2/N)$.
2. *Determine the ideal collar angle and ideal number of collars.* The ideal angle between two collars is

$$\delta_I := \sqrt{4\pi/N}.$$

The ideal number of collars between the polar caps, all of which have angle δ_I , is

$$n_I := \frac{\pi - 2\phi_c}{\delta_I}.$$

3. *Determine the actual number of collars, n .* If $N = 2$, then $n := 0$. Otherwise,

$$n := \max\{1, \text{round}(n_I)\}.$$

4. *Create a list of the ideal number of cells in each collar.* The “fitting” collar angle is

$$\delta_F := \frac{n_I}{n} \delta_I = \frac{\pi - 2\phi_c}{n}.$$

Label the collars $\{C_j\}_{j=1}^{n+2}$ southward with the North polar cap as C_1 and the South polar cap as C_{n+2} . The area A_j of collar C_j can be written as the difference of polar cap areas:

$$A_j = 2\pi(\cos(\phi_c + (j-2)\delta_F) - \cos(\phi_c + (j-1)\delta_F)).$$

Thus the ideal number of cells $y_{j,I}$ in each collar C_j , $j \in \{2, \dots, n+1\}$, is given by

$$y_{j,I} = \frac{4\pi A_j}{N}.$$

5. *Create a list of the actual number of cells in each collar.* We apply a cumulative rounding procedure. Letting y_j be the number of cells in C_j , define the sequences y and a by $a_1 := 0$, $y_1 := 1$, and for $j \in \{2, \dots, n+1\}$:

$$y_j := \text{round}(y_{j,I} + a_{j-1}), \quad a_j := \sum_{k=1}^j y_k - y_{k,I}.$$

6. *Create a list of latitudes ϕ_j of each collar and partition each collar into cells.* We define ϕ_j as follows: $\phi_0 = 0$, $\phi_{n+2} = \pi$ and for $j \in \{1, \dots, n+1\}$,

$$\phi_j = \cos^{-1}\left(1 - \frac{2}{N} \sum_{k=1}^j y_k\right).$$

Thus the North polar cap of radius ϕ_j has normalized area $\sum_{k=1}^j y_k/N$, and $C_j := R([\phi_{j-1}, \phi_j] \times [0, 2\pi])$.

7. *Partition each collar into cells.* C_j has y_j equal cells

$$\left\{ R([\phi_{j-1}, \phi_j] \times [\theta_j + k\frac{y_j}{2\pi}, \theta_j + (k+1)\frac{y_j}{2\pi}]) \right\}_{k=0}^{y_j-1},$$

where $\theta_j \in [0, 2\pi)$ can be chosen to be any starting angle. Note that because θ_j are chosen independently, the equal area partition determined by the algorithm is not unique. Indeed, the collars can rotate past each other without affecting the diameter bound or equal area property of the partition. Because the choice of the θ_j 's does not strongly affect the other properties with which we are concerned, we will take them to be random.

The point set ω_N is defined to be the centers of the cells of the rectilinear partition. As proved by Zhou [67], the cells are diameter bounded from above by $7/\sqrt{N}$; however, numerical experiments from Leopardi in [36] suggest the bound to be $6.5/\sqrt{N}$. For large N , the zonal equal area configurations look very similar to the generalized spiral configurations. Namely they exhibit isolatitudinal rings with separation between adjacent points equal to separation between rings and a random longitudinal shift between points in adjacent rings. As shown in Section 3, the energy computations for both point sets are nearly identical.

Proposition 3. *The sequence of zonal equal area configurations is equidistributed and quasi-uniform.*

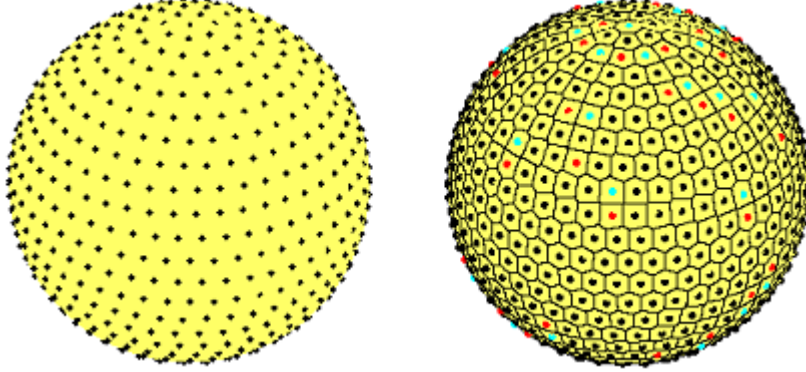


Figure 8: Zonal equal area points for $N = 700$ and corresponding Voronoi decomposition. The configurations have a similar structure to the generalized spiral points in Figure 2.

Table 3: Mesh Ratios for Zonal Equal Area Nodes

N	$\gamma(\omega_N)$	N	$\gamma(\omega_N)$	N	$\gamma(\omega_N)$
10	0.711934	400	0.769527	20000	0.758100
20	0.790937	500	0.766808	30000	0.758069
30	0.788546	1000	0.765356	40000	0.756793
40	0.843385	2000	0.764631	50000	0.756785
50	0.790252	3000	0.758645	100000	0.756770
100	0.761296	4000	0.756510	200000	0.756762
200	0.764846	5000	0.764217	300000	0.758015
300	0.763188	10000	0.758192	500000	0.756757

The above construction was modified by Bondarenko et al [8] to create a partition with geodesic boundaries for the creation of well-separated spherical designs. More details can be found in [8]. Table 3 gives a comparison of the mesh ratios of the zonal points.

HEALPix Nodes

Developed by NASA for fast data analysis of the cosmic microwave background (CMB), the Hierarchical Equal Area iso-Latitude Pixelization (HEALPix) was designed to have three properties essential for computational efficiency in discretizing functions on \mathbb{S}^2 and processing large amounts of data [30]:

1. The sphere is hierarchically tessellated into curvilinear quadrilaterals.
2. The pixelization is an equal area partition of \mathbb{S}^2 .
3. The point sets are distributed along fixed lines of latitude.

To create the partition of \mathbb{S}^2 , the authors in [30] first divide the sphere into 12 equal area, four sided pixels defined by the following boundaries:

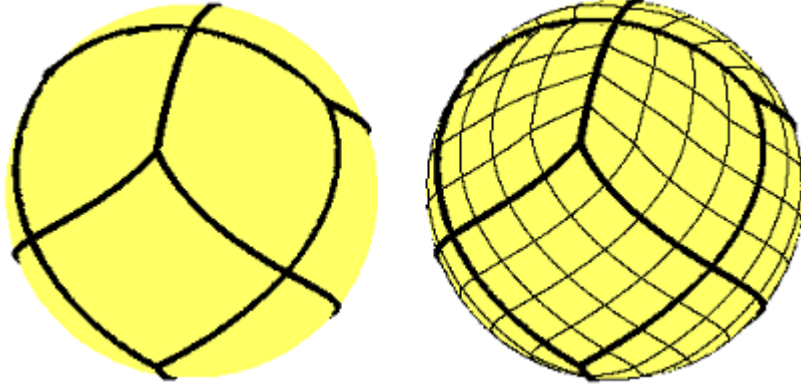


Figure 9: Base tessellation of the sphere into 12 equal area pixels. A finer mesh is created by dividing each base pixel into a $k \times k$ grid of equal area subpixels of the same shape. The HEALPix points are taken to be the centers of the pixels.

$$|\cos \phi| > \frac{2}{3}, \quad \theta = m\frac{\pi}{2}, \quad m = 0, 1, 2, 3$$

$$\cos \phi = \frac{-2 - 4m}{3} + \frac{8\theta}{3\pi}, \quad \frac{m\pi}{2} \leq \theta \leq \frac{(m+1)\pi}{2}, \quad m = 0, 1, 2, 3$$

$$\cos \phi = \frac{2 - 4m}{3} - \frac{8\theta}{3\pi}, \quad \frac{-(m+1)\pi}{2} \leq \theta \leq \frac{-m\pi}{2}, \quad m = 0, 1, 2, 3.$$

The base tessellation is shown in Figure 9. For a given $k \in \mathbb{N}$, each pixel is partitioned into a $k \times k$ grid of sub-pixels of the same shape and equal area. The HEALPix point sets are taken to be the centers of these pixels.

On the polar regions $|\cos \phi| > 2/3$, the points are distributed along k iso-latitudinal rings, indexed by i , each with $4i$ equally spaced points, indexed by j :

$$|\cos \phi_i| = 1 - \frac{i^2}{3k^2}, \quad \theta_j = \frac{\pi}{2i} \left(j - \frac{1}{2} \right).$$

On the equatorial region, there are $2k - 1$ iso-latitudinal rings, each with $4k$ points. The rings are indexed by $k \leq |i| \leq 2k$ and the points by $1 \leq j \leq 4k$:

$$|\cos \phi_i| = \frac{4}{3} - \frac{2i}{3k},$$

$$\theta_j = \frac{\pi}{2k} \left(j - \frac{s}{2} \right), \quad s = (i - k + 1) \mod 2.$$

The index s describes the phase shift between rings. This gives a configuration of size $N = 12k^2$. The point sets are hierarchical along the subsequence $k = 3^m$. Holhoş and Roşca [32] have shown that the HEALPix points can be obtained as the image of points on a certain convex polyherdon under an area preserving mapping to the sphere.

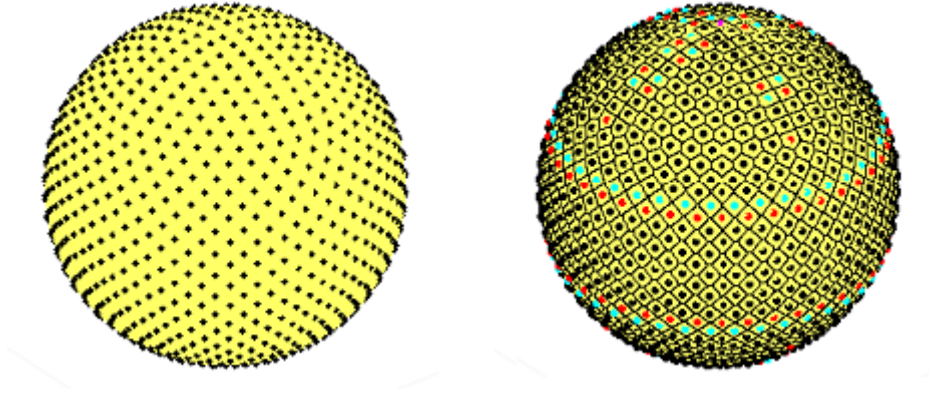


Figure 10: HEALPix nodes and Voronoi decomposition for $N = 1200, k = 10$.

Proposition 4. *The sequence of HEALPix configurations is equidistributed and quasi-uniform.*

Numerically, the mesh ratio appears to be bounded by 1, as shown in Table 4.

Table 4: Mesh Ratios for HEALPix nodes

k	N	$\gamma(\omega_N)$	k	N	$\gamma(\omega_N)$	k	N	$\gamma(\omega_N)$
1	12	0.864783	9	972	0.965950	45	24300	0.992956
2	48	0.862243	10	1200	0.969599	50	30000	0.993648
3	108	0.909698	15	2700	0.979371	60	43200	0.994701
4	192	0.929080	20	4800	0.984328	70	58800	0.995456
5	300	0.940016	25	7500	0.987365	80	76800	0.996020
6	432	0.951047	30	10800	0.989509	90	97200	0.996455
7	588	0.957584	35	14700	0.990959	100	120000	0.996807
8	768	0.961782	40	19200	0.992082	150	270000	0.997867

Polyhedral Nodes and Area Preserving Maps

Another class of point sets are those derived from subdividing regular polyhedra and applying radial projection: $\Pi(\mathbf{x}) = \mathbf{x}/\|\mathbf{x}\|$ or an equal area projection. These node sets are used in finite element methods to give low error solutions to boundary value problems. See, for instance, [28] and [43].

Radial Icosahedral Nodes

This point set, as described in [60] and [66] is formed by overlaying a regular triangular lattice onto each face of a regular icosahedron of circumradius 1 and edge length $a = \csc(2\pi/5)$. Given $k \in \mathbb{N}$, for each vertex v , divide two adjacent edges emanating from v into basis vectors of length a/k . For the face \mathcal{F} determined by these edges and vertex, the icosahedral point set $\widetilde{\omega}_{N_k}$ on \mathcal{F} is taken to be the set of lattice points generated by these basis vectors restricted

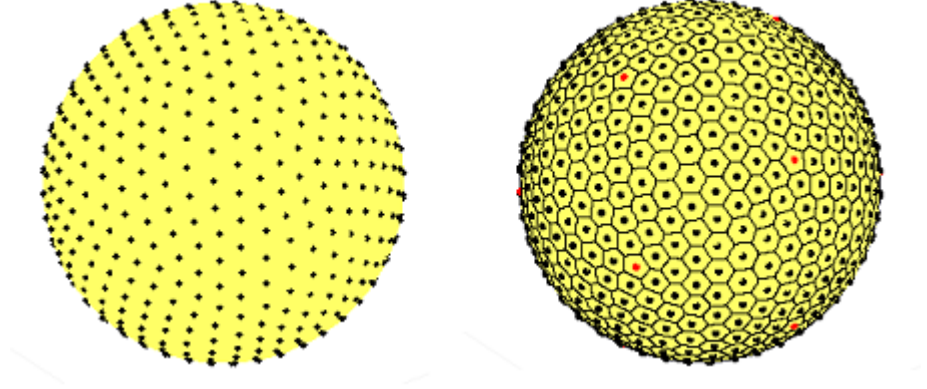


Figure 11: Radial icosahedral nodes $N = 642$. The Voronoi decomposition is composed of regular hexagons of varying size and 12 pentagons at the vertices of the icosahedron.

to \mathcal{F} . The spherical points are $\omega_{N_k} := \Pi(\widetilde{\omega_{N_k}})$. These node sets are defined for total points $N = 10k^2 + 2$ and hierarchical along the subsequence $k_j = k_0 2^j$ for any $k_0 \in \mathbb{N}$.

The sequence of icosahedral configurations $\{\widetilde{\omega_{N_k}}\}_{k=1}^\infty$ is equidistributed. However, because radial projection is not area preserving, the sequence of spherical configurations is not equidistributed. Density is higher towards the vertices of the icosahedron and lower towards the center of the faces where the areal distortion of Π is greatest. The Voronoi decomposition of ω_{N_k} is composed of twelve regular pentagons with all other cells regular hexagons of varying size as illustrated in Figure 11.

Proposition 5. *The sequence of radial icosahedral configurations is quasi-uniform.*

Numerically, the mesh ratio appears to be bounded by 0.86, as shown in Table 5.

Table 5: Mesh Ratios for Radial Icosahedral Nodes

k	N	$\gamma(\omega_N)$	k	N	$\gamma(\omega_N)$
1	12	0.620429	20	4002	0.830750
2	42	0.667597	30	9002	0.838066
3	92	0.684698	40	16002	0.842358
4	162	0.745348	50	25002	0.844697
5	252	0.765157	60	36002	0.846156
6	362	0.769854	70	49002	0.847376
7	492	0.789179	100	100002	0.849390
10	1002	0.808024	150	225002	0.850941
15	2252	0.821504	200	400002	0.851745

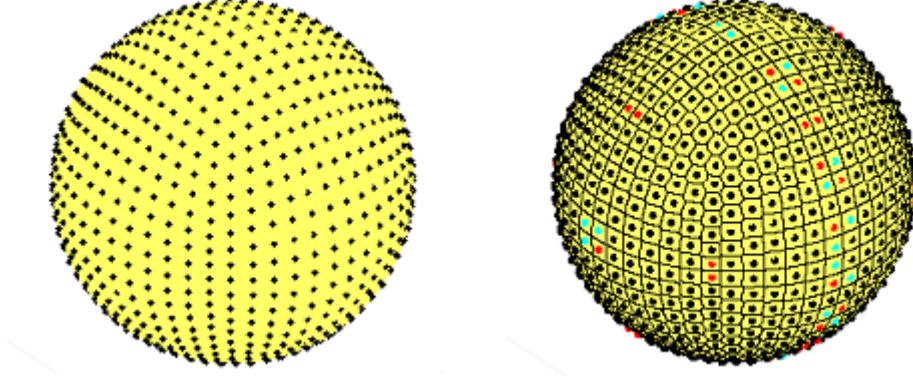


Figure 12: Plot of $N = 1016$ Cubed Sphere Points and Voronoi Decomposition. The Voronoi cells tend towards regular hexagons near the vertices of the cube. Towards the middle of each face they resemble a square lattice.

Cubed Sphere Nodes

A similar method as above can be applied to the cube [43]. A square $k \times k$ grid is placed on each face of the cube and radially projected to the sphere. A typical point set is shown in Figure 12. The configurations are defined for $N = 6k^2 - 12k + 8$ and are hierarchical along the subsequence $k = k_0 2^m$. By an argument similar to that in Proposition 5, the limiting distribution is not uniform, but the sequence of configurations is quasi-uniform. Numerically, the mesh ratio seems to quickly converge to 1, as shown in Table 6.

Table 6: Mesh Ratios for Cubed Sphere Points

k	N	$\gamma(\omega_N)$	k	N	$\gamma(\omega_N)$	k	N	$\gamma(\omega_N)$
2	8	0.827329	10	488	0.996846	50	14408	0.999893
3	26	0.794265	15	1178	0.994025	60	20888	0.999926
4	56	0.972885	20	2168	0.999289	70	28568	0.999946
5	98	0.933655	25	3458	0.997954	80	37448	0.999959
6	152	0.989913	30	5048	0.999695	90	47528	0.999968
7	218	0.968757	35	6938	0.998979	100	58808	0.999974
8	296	0.994805	40	9128	0.999831	150	133208	0.999988
9	386	0.982046	45	11618	0.999390	200	237608	0.999994

Octahedral Points

Unlike in the previous examples, the octahedral points, described by Holhos and Roşca [33], are derived from an area preserving map \mathcal{U} from the regular octahedron \mathbb{K} of edge length $L = \sqrt{2\pi}/\sqrt[4]{3}$ and surface area 4π to \mathbb{S}^2 . Let $\mathcal{U}_x, \mathcal{U}_y$, and \mathcal{U}_z denote the x, y , and z components of \mathcal{U} respectively. For $(X, Y, Z) \in \mathbb{K}$,

$$\mathcal{U}_z = \frac{2Z}{L^2}(\sqrt{2}L - |Z|),$$

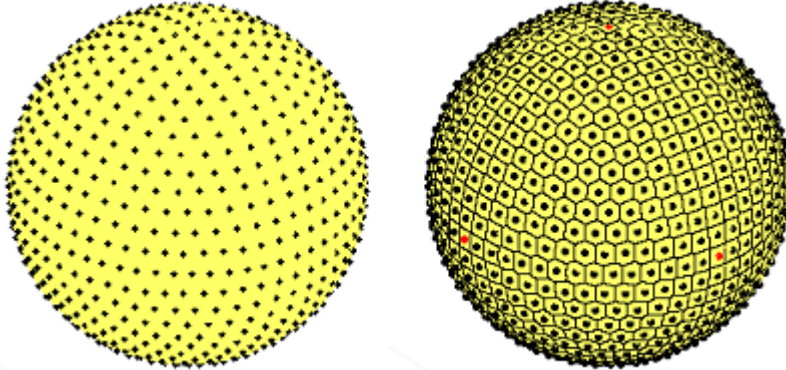


Figure 13: Equal area octahedral points for $k = 15$ and $N = 902$. The Voronoi decomposition of the octahedral points is composed of hexagons and 8 squares at the vertices of the octahedron. The hexagons approach regularity towards the center of the faces and deform along the edges.

$$\mathcal{U}_x = \text{sgn}(X) \sqrt{1 - \mathcal{U}_z^2} \cos \frac{\pi|Y|}{2(|X| + |Y|)},$$

$$\mathcal{U}_y = \text{sgn}(Y) \sqrt{1 - \mathcal{U}_z^2} \sin \frac{\pi|Y|}{2(|X| + |Y|)}.$$

To produce a spherical point set, the authors form a partition P_k of k^2 triangles on each face of the octahedron in the same manner as the radial icosahedral points and obtain an equal area spherical partition $\mathcal{P}_k = \mathcal{U}(P_k)$. The point sets ω_{N_k} are taken to be the vertices of the triangles of \mathcal{P}_k . For a given k , there are $8k^2$ triangles and $N = 4k^2 + 2$ points.

The octahedral configurations have similar properties to the HEALPix node sets. They are iso-latitudinal and hierarchical along the subsequence $k = k_0 2^m$. The sequence of configurations is equidistributed, and in addition, the authors in [33] compute a diameter bound for any triangular region \mathcal{T} of \mathcal{P}_k to be

$$\text{diam } \mathcal{T} \leq \frac{2\sqrt{4 + \pi^2}}{\sqrt{8k^2}} \approx \frac{7.448}{\sqrt{8k^2}}.$$

Following their proof of this bound, we can calculate a lower bound on the separation and an upper bound on the mesh norm.

Theorem 6. *The sequence of equal area octahedral configurations is quasi-uniform with*

$$\gamma(\omega_{4k^2+2}) \leq \frac{1}{4} \sqrt{\frac{4 + \pi^2}{2 - (k+1)^2/k^2}} \rightarrow \frac{\sqrt{4 + \pi^2}}{4} \approx 0.931048..., \quad k \rightarrow \infty. \quad (11)$$

This bound seems to be near optimal. As shown in Table 7, the mesh ratio grows to at least 0.9235.

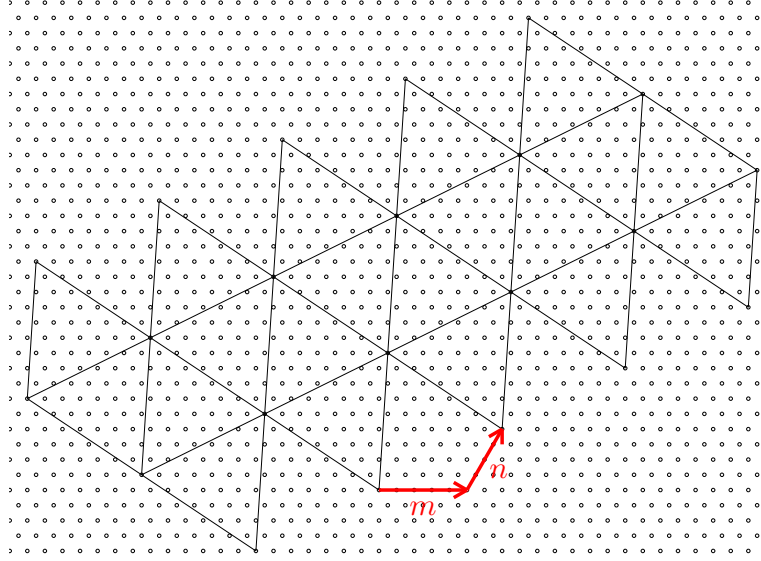


Figure 14: Planar icosahedral mesh for $(m, n) = (5, 4)$.

Table 7: Mesh Ratios for Octahedral Nodes

k	N	$\gamma(\omega_N)$	k	N	$\gamma(\omega_N)$	k	N	$\gamma(\omega_N)$
1	6	0.675511	9	326	0.873510	60	14402	0.905758
2	18	0.872884	10	402	0.875606	70	19602	0.908047
3	38	0.854610	15	902	0.882510	80	25602	0.909875
4	66	0.856329	20	1602	0.886310	90	32402	0.911382
5	102	0.860536	25	2502	0.888702	100	40002	0.912644
6	146	0.864599	30	3602	0.892884	200	160002	0.919218
7	198	0.868095	40	6402	0.898762	300	360002	0.921947
8	258	0.871036	50	10002	0.902784	400	640002	0.923503

Mesh Icosahedral Equal Area Points

Improvements to the radially projected icosahedral points have been put forth by Song et al [56] and Tegmark [61]. Here, we introduce two other improvements to these points to create new configurations. First, we generalize the icosahedral lattice structure to create configurations of more possible numbers of total points. Due to a method of Caspar and Klug [21] derived during their investigation of the construction of viruses, we define a triangular lattice on a regular icosahedron with total points

$$N = 10(m^2 + mn + n^2) + 2, \quad (m, n) \in \mathbb{N} \times \mathbb{N} \setminus (0, 0).$$

Consider the planar triangular lattice generated by $e_1 = (1, 0)$ and $e_2 = (1/2, \sqrt{3}/2)$. For a given (m, n) , let $e_{m,n} = me_1 + ne_2$ and it's rotation by $\pi/3$

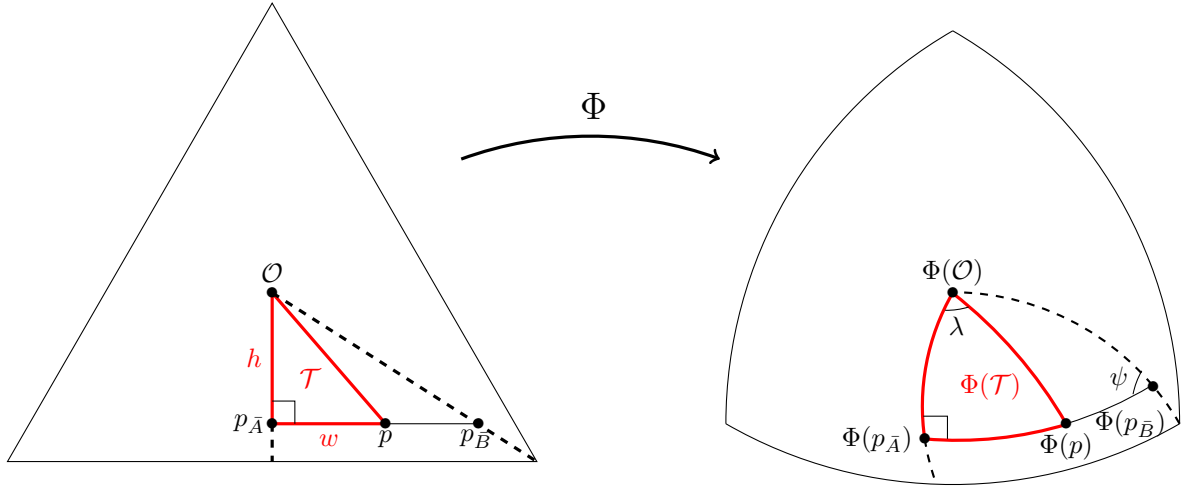


Figure 15: Illustration of area preserving map Φ defined piecewise on each triangle bounded by two altitudes of a face with relevant variables labeled.

be basis vectors for an unfolded icosahedron superimposed on the lattice. This is illustrated in Figure 14. Folding the icosahedron results in a triangular lattice $\widetilde{\omega}_N$ on each face. Due to rotational symmetry of the lattice, the resulting configuration is independent of how the icosahedron is unfolded. The subsequence $(m, 0)$ produces the lattice for the radial icosahedral nodes.

Secondly, we derive an area preserving map Φ from the regular icosahedron \mathcal{I} of edge length $L = \sqrt{4\pi}/\sqrt[4]{75}$, circumradius $r = L \sin 2\pi/5$, and surface area 4π using the technique presented by Snyder [54] for the truncated icosahedron. We define Φ piecewise by dividing each face $\mathcal{F} \subset \mathcal{I}$ into the six triangles \mathcal{R}_i partitioned by the altitudes of \mathcal{F} :

1. Parametrize each point $p \in \mathcal{R}_i$ by h and w as labeled in Figure 15. If \bar{A} is the side of \mathcal{R}_i of length $L/2\sqrt{3}$, then w is the distance from p to \bar{A} and h is the distance of $p_{\bar{A}} := \text{proj}(p, \bar{A})$ to \mathcal{O} , the center of \mathcal{F} .

2. Let \bar{B} be the side of \mathcal{R}_i of length $L/\sqrt{3}$ and $p_{\bar{B}}$ be the intersection of the line $\overline{p_{\bar{A}}p}$ with \bar{B} . For the triangle $\mathcal{S} = \triangle p_{\bar{A}}p_{\bar{B}}\mathcal{O}$, find ψ as in Figure 15 and spherical right triangle $\Phi(\mathcal{S})$ such that $\text{Area}(\mathcal{S}) = \sigma(\Phi(\mathcal{S})) = \psi - \pi/6$. Thus,

$$\psi = \frac{h^2\sqrt{3}}{2} + \frac{\pi}{6}.$$

3. $\Phi(p)$ will lie on the great circle $\Phi(\overline{p_{\bar{A}}p_{\bar{B}}})$. Letting $\mathcal{T} = \triangle p_{\bar{A}}p, \mathcal{O}$, find λ as in Figure 15 such that $\text{Area}(\mathcal{T}) = \sigma(\Phi(\mathcal{T}))$. By the spherical law of cosines,

$$\sigma(\Phi(\mathcal{T})) = \lambda + \cos^{-1} \left(\frac{2 \sin \lambda \cos \psi}{\sqrt{3}} \right) - \frac{\pi}{2}.$$

Thus

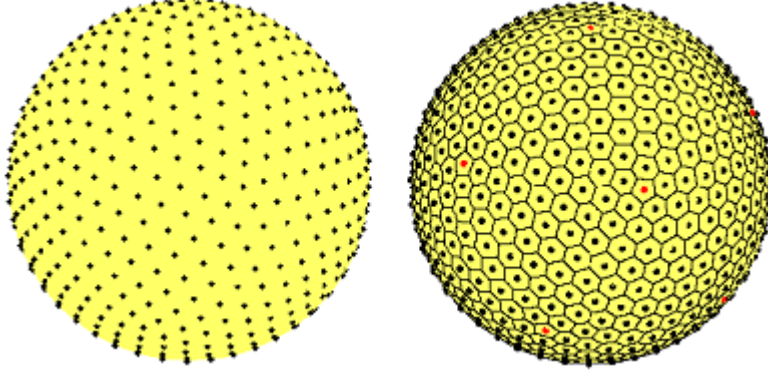


Figure 16: Equal area mesh icosahedral nodes for $(m, n) = (7, 2)$ and total points $N = 672$. The Voronoi decomposition forms a spherical Goldberg polyhedron.

Table 8: Mesh Ratios for Equal Area Icosahedral Nodes

(m, n)	N	$\gamma(\omega_N)$	(m, n)	N	$\gamma(\omega_N)$	(m, n)	N	$\gamma(\omega_N)$
(1,0)	12	0.620429	(7,1)	572	0.688031	(37,27)	30972	0.730733
(1,1)	32	0.617964	(7,5)	1092	0.707058	(40,33)	40092	0.732326
(2,0)	42	0.667598	(12,4)	2082	0.706688	(42,40)	50442	0.732529
(2,1)	72	0.657081	(16,3)	3132	0.704123	(65,50)	99752	0.733719
(3,0)	92	0.659610	(16,7)	4172	0.717067	(90,75)	204752	0.735013
(3,1)	132	0.668227	(19,6)	5112	0.712681	(100,100)	300002	0.735397
(4,1)	212	0.680153	(19,18)	10272	0.726243	(131,100)	402612	0.735592
(5,2)	392	0.687368	(31,21)	20532	0.728761	(145,115)	509252	0.735965

$$\tan \lambda = \frac{\sin(\frac{hw}{2})}{\cos(\frac{hw}{2}) - \frac{2 \cos \psi}{\sqrt{3}}}.$$

4. Transform (ψ, λ) into spherical coordinates.

The map Φ is extended to \mathcal{I} by rotations and reflections. This defines the unique azimuthal equal area projection from \mathcal{I} onto \mathbb{S}^2 [55]. The spherical configurations are $\omega_N := \Phi(\widetilde{\omega}_N)$. A typical point set is shown in Figure 16. The Voronoi cells are almost regular hexagons with 12 pentagonal cells at the vertices of \mathcal{I} , and the Voronoi decomposition forms a spherical Goldberg Polyhedron [29]. To implement the points in Matlab, we derive explicit formulas on a triangular face. More details are provided in the companion paper [42].

Unlike the radial icosahedral points, the sequence of equal area configurations is equidistributed. Regarding quasi-uniformity, the following is proved in [42].

Proposition 7. *The sequence of equal area icosahedral configurations are quasi-uniform with*

$$\gamma(\omega_N) \leq 0.798....$$

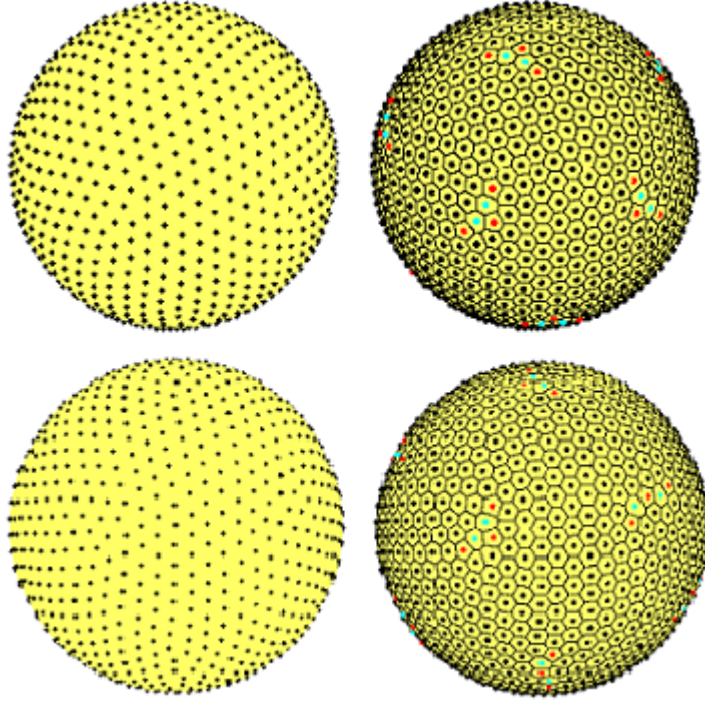


Figure 17: Coulomb points (top) and log points (bottom) and their Voronoi decomposition for $N = 1024$. The structure is very similar for both.

As shown in Table 8, the mesh ratios appears to stay below 0.736. These are the lowest mesh ratios of all point sets discussed.

Coulomb Points and Log Energy Points (Elliptic Fekete Points)

For $s = 1$, Riesz s -energy minimization is the classic Thomson problem for the Coulomb potential [62]. The sequence of minimal Coulomb energy configurations is known to be equidistributed, well-separated, and quasi-uniform [24]. However, no explicit bound is known for the mesh ratio. The Voronoi decomposition of these cells, as shown in Figure 17, primarily consists of close to regular hexagons with heptagons and pentagons forming scars along the sphere. For relatively small N , the scars grow out from the 12 vertices of the icosahedron like dislocations in a crystal due to displacement deformities. For $N > 5,000$, the scars become less fixed, spreading across the sphere. For an in-depth discussion of the scarring behavior, see Bowick et al [11] and [12].

The log energy points are minimizers of the Riesz logarithmic potential. The sequence of log energy configurations is known to be equidistributed and well-separated, but covering and quasi-uniformity is an open problem. As shown in Table 9 below, numerically the log energy points appear to be quasi-uniform. The best known lower bound on separation is due to Dragnev [26]:

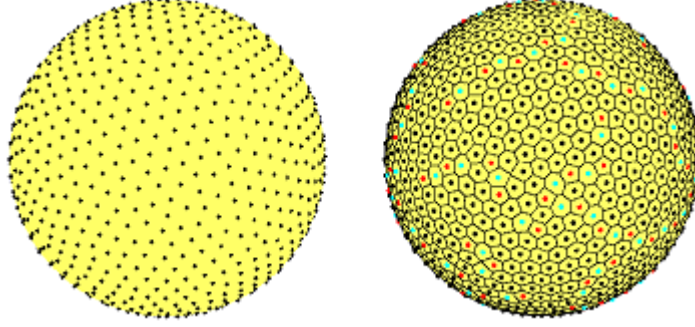


Figure 18: Maximal determinant nodes for $N = 961$. The Voronoi decomposition is primarily composed of regular hexagons with scarring features similar to the minimal energy points.

$$\delta(\omega_N^{\log}) \geq \frac{2}{\sqrt{N}}, \quad N \geq 2.$$

Their geometric structure is very similar to the Coulomb points as shown in Figure 17. The energies of log and Coulomb points have the same asymptotic behavior in the dominant and second order term for many Riesz potentials. See Section 3 and Conjecture 22.

Generating these points is a highly nonlinear optimization problem. Unlike the configurations we have described up to now, they are not so quickly obtained. Table 9 displays the mesh ratios of near minimal Coulomb and log energy configurations. We remark that the sequence appears to have outliers at several values of N , such as $N = 20, 300$, and 4096 . Points for $N < 500$ and $N = k^2$, $k \leq 150$, were provided by Rob Womersley.

Table 9: Mesh Ratios for Coulomb and Log Energy Points

N	$\gamma(\omega_N^{\log})$	$\gamma(\omega_N^{\text{Coul}})$	N	$\gamma(\omega_N^{\log})$	$\gamma(\omega_N^{\text{Coul}})$
10	0.687401	0.689279	500	0.757354	0.755834
20	0.731613	0.733265	1024	0.752122	0.755770
30	0.695481	0.692966	2025	0.761261	0.766218
40	0.669531	0.670842	3025	0.765075	0.761661
50	0.661301	0.656591	4096	0.770240	0.765712
100	0.695371	0.694604	5041	0.753573	0.758457
200	0.662102	0.658561	10000	0.762672	0.761964
300	0.740635	0.730182	15129	0.762385	0.763398
400	0.650106	0.647351	22500	0.773483	0.767096

Maximal Determinant Nodes (Fekete Nodes)

Other node sets used in polynomial interpolation and numerical integration on the sphere are the maximal determinant nodes. Let $\phi_1, \dots, \phi_{(n+1)^2}$ be a basis

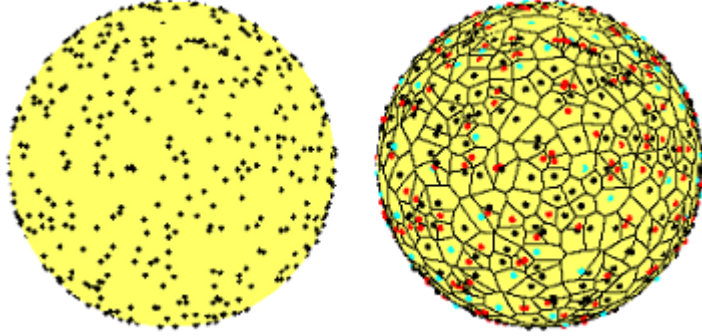


Figure 19: Random points for $N = 700$ and their Voronoi decomposition.

for the space $\mathbb{P}_n(\mathbb{S}^2)$ of spherical polynomials of degree $\leq n$. The maximal determinant node set is the configuration $\omega_N := \omega_{(n+1)^2} \subset \mathbb{S}^2$ which maximizes

$$\det(\phi_i(x_j))_{i,j=1}^{(n+1)^2}$$

These points are independent of the choice of basis. The interpolatory cubature rule associated with the configuration ω_N ,

$$Q_n(f) := \sum_{j=1}^N w_j f(x_j),$$

is conjectured in [52] to have all weights positive which is of interest in numerical integration. For more information about these points and their applications, see [48], [49], and [52]. A typical node set is shown in Figure 18.

Like the minimal energy nodes, computing the maximal determinant nodes is a nonlinear optimization problem. The maximum is approximated by conjugate gradient and Newton-like methods on \mathbb{S}^2 [52]. Nodes for $1 \leq n \leq 165$ are available from <http://web.maths.unsw.edu.au/~rsw/Sphere/Extremal/New/index.html>.

Berman et al [5] proved the sequence of maximal determinant configurations is equidistributed, while in [52], Sloan and Womersley proved it is quasi-uniform with

$$\limsup_{N \rightarrow \infty} \gamma(\omega_N) < \frac{4j_0}{\pi} \approx 3.06195,$$

where j_0 is the smallest positive zero of the Bessel function of the first kind, J_0 . As shown in Table 10, the mesh ratio bound appears to be much lower though it is unclear whether or not $\lim_{N \rightarrow \infty} \gamma(\omega_N)$ exists.

Random Points

The final configurations we consider are random configurations ω_N^{rand} consisting of N independent samples chosen with respect to surface area measure. Not surprisingly, these configurations do not have optimal order separation or covering and the sequence is not quasi-uniform. As proved in [18] and [50] respectively,

Table 10: Mesh Ratios for Maximal Determinant Nodes

N	$\gamma(\omega_N)$	N	$\gamma(\omega_N)$
9	0.718884	625	0.805608
16	0.685587	1024	0.840506
25	0.768510	2025	0.858874
36	0.806140	3025	0.847347
49	0.777490	4096	0.859887
100	0.708579	4900	0.877990
225	0.860728	10201	0.859625
324	0.799227	15129	0.865695
400	0.809172	22500	0.881492

$$\lim_{N \rightarrow \infty} \mathbb{E}(\delta(\omega_N^{\text{rand}}))N = \sqrt{2\pi}, \quad \lim_{N \rightarrow \infty} \mathbb{E}(\eta(\omega_N^{\text{rand}})) \left(\frac{N}{\log N} \right)^{1/2} = 2.$$

Note that while the order of the separation of random points is off by factor of $N^{1/2}$, the covering is only off by a factor of $(\log N)^{1/2}$. Figure 19 shows a realization of i.i.d. uniformly chosen random points on \mathbb{S}^2 .

Summary of Properties

The following tables compare some of the properties of the point sets described above. Table 11 compares which sequences are proven to be equidistributed and well-separated, for which values of N the configurations are defined, and whether a subsequence is hierarchical. Table 12 compares which sequences are quasi-uniform and the numerically determined bounds for separation and mesh ratio constants.

3 Asymptotic Energy Considerations

We now turn our attention to the potential energy of the above configurations, in particular, $E_{\log}(\omega_N)$ and $E_s(\omega_N)$ for $s = -1, 1, 2$, and 3 . We are interested in the asymptotic behavior of the energies for above configurations as $N \rightarrow \infty$ and how well the leading terms in the expansion of their energies match the known or conjectured leading terms and coefficients in the minimal energy expansion. We begin with the following well known necessary condition for asymptotically optimal point sets [10].

Theorem 8. *Let $\{\omega_N\}_{N=2}^\infty$ be a sequence of configurations that is asymptotically optimal with respect to logarithmic energy or Riesz s -energy for some $s > -2$, $s \neq 0$, i.e.,*

$$\lim_{N \rightarrow \infty} \frac{E_s(\omega_N)}{\mathcal{E}_s(N)} = 1 \quad \text{or} \quad \lim_{N \rightarrow \infty} \frac{E_{\log}(\omega_N)}{\mathcal{E}_{\log}(N)} = 1.$$

Then $\{\omega_N\}_{N=2}^\infty$ is equidistributed.

Table 11: Summary of Point Set Properties

Name	Defined for	Hier.	Equidist.	Separated
Gen Spiral	$N \geq 2$	No	Yes	Yes
Fibonacci	Odd N	No	Yes	Yes
Hammersley	$N \geq 2$	No	Yes	No
Zonal Eq. Area	$N \geq 2$	No	Yes	Yes
HEALPix	$12k^2$,	Subseq.	Yes	Yes
Octahedral	$4k^2 + 2$	Subseq.	Yes	Yes
Radial Icos.	$10k^2 + 2$,	Subseq.	No	Yes
Cubed Sphere	$6k^2 - 12k + 8$	Subseq.	No	Yes
Equal Area Icos.	$10(m^2 + mn + n^2) + 2$	Subseq.	Yes	Yes
Coulomb	$N \geq 2$	No	Yes	Yes
Log Energy	$N \geq 2$	No	Yes	Yes
Max Det.	$(1 + k)^2$	No	Yes	Yes
Random	$N \geq 2$	No	Yes	No

Table 12: Comparison of Separation and Mesh Ratio Constants

Name	Quasi-Uniform	Numeric lower bound on $\liminf \delta(\omega_N)\sqrt{N}$	Numeric upper bound on $\limsup \gamma(\omega_N)\sqrt{N}$
Gen Spiral	Yes	3.1319	0.8099
Fibonacci	Yes	3.0921	0.8823
Hammersley	No	N/A	N/A
Zonal Eq. Area	Yes	3.3222	0.7568
HEALPix	Yes	2.8345	1.0000
Radial Icos.	Yes	2.8363	0.8517
Cubed Sphere	Yes	2.7027	1.0000
Octahedral	Yes	2.8284	0.9235
Equal Area Icos.	Yes	3.1604	0.7360
Coulomb	Yes	3.3794	0.7671
Log Energy	Conj.	3.3733	0.7735
Max Det.	Yes	3.1957	0.8900
Random	No	N/A	N/A

We define the energy of a probability measure μ on \mathbb{S}^2 with respect to the logarithmic or Riesz s -potential as

$$\mathcal{I}_s[\mu] := \int \int \frac{1}{|\mathbf{x} - \mathbf{y}|^s} d\mu(\mathbf{x}) d\mu(\mathbf{y}), \quad s \neq 0$$

$$\mathcal{I}_{\log}[\mu] := \int \int \log \frac{1}{|\mathbf{x} - \mathbf{y}|} d\mu(\mathbf{x}) d\mu(\mathbf{y}).$$

The normalized surface area measure σ is the unique minimizer of $\mathcal{I}_{\log}[\mu]$ and $\mathcal{I}_s[\mu]$ for $-2 < s < 2$, $s \neq 0$, and

$$\mathcal{I}_{\log}[\sigma] = \frac{1}{2} - \log 2,$$

$$\mathcal{I}_s[\sigma] = \frac{2^{1-s}}{2-s}, \quad -2 < s < 2.$$

However, for $s \geq 2$, $\mathcal{I}_s[\mu] = \infty$ for all μ supported on \mathbb{S}^2 (see for example [10]).

For random points, the expected value of the s -energy is easily computed:

$$\mathbb{E}[E_s(\omega_N^{\text{rand}})] = \mathcal{I}_s[\sigma](N(N-1)), \quad -2 < s < 2. \quad (12)$$

For $s \geq 2$, $\mathbb{E}[E_s(\omega_N^{\text{rand}})] = \infty$.

The Epstein-Zeta function for a lattice Λ in \mathbb{R}^2 is given by

$$\zeta_\Lambda(s) := \sum_{0 \neq \mathbf{x} \in \Lambda} |\mathbf{x}|^{-s}, \quad \text{Re } s > 2.$$

Let Λ_2 be the regular triangular lattice in \mathbb{R}^2 generated by basis vectors $(1, 0)$ and $(1/2, \sqrt{3}/2)$. It is known from number theory that $\zeta_{\Lambda_2}(s)$ admits the factorization

$$\zeta_{\Lambda_2}(s) = 6\zeta(s/2)L_{-3}(s/2), \quad \text{Re } s > 2, \quad (13)$$

where

$$L_{-3}(s) := 1 - \frac{1}{2^s} + \frac{1}{4^s} - \frac{1}{5^s} + \frac{1}{7^s} - \dots, \quad \text{Re } s > 1,$$

is a Dirichlet L-series. The right-hand side of (13) can be used to extend $\zeta_{\Lambda_2}(s)$ to s with $\text{Re } s < 2$.

3.1 Logarithmic Potential

The following asymptotic expansion is proven by Betermin and Sandier in [6]:

Theorem 9. *There exists a constant $C \neq 0$, independent of N , such that*

$$\mathcal{E}_{\log}(N) = \mathcal{I}_{\log}[\sigma]N^2 - \frac{N \log N}{2} + CN + o(N), \quad N \rightarrow \infty,$$

$$-0.22553754 \leq C \leq \hat{C} := 2 \log 2 + \frac{1}{2} \log \frac{2}{3} + 3 \log \frac{\sqrt{\pi}}{\Gamma(1/3)} = -0.05560530\dots$$

The following extension of Theorem 9 is conjectured by Brauchart et al in [17]:

Conjecture 10.

$$\mathcal{E}_{\log}(N) = \mathcal{I}_{\log}[\sigma]N^2 - \frac{N \log N}{2} + \hat{C}N + D \log N + O(1), \quad N \rightarrow \infty.$$

Beltran [4] provides a partial converse to Theorem 8:

Theorem 11. *If $\{\omega_N\}_{N=2}^\infty$ is a sequence of well-separated configurations whose spherical cap discrepancy satisfies*

$$\lim_{N \rightarrow \infty} D_C(\omega_N) \log N = 0,$$

then $\{\omega_N\}_{N=2}^\infty$ are asymptotically optimal with respect to logarithmic energy.

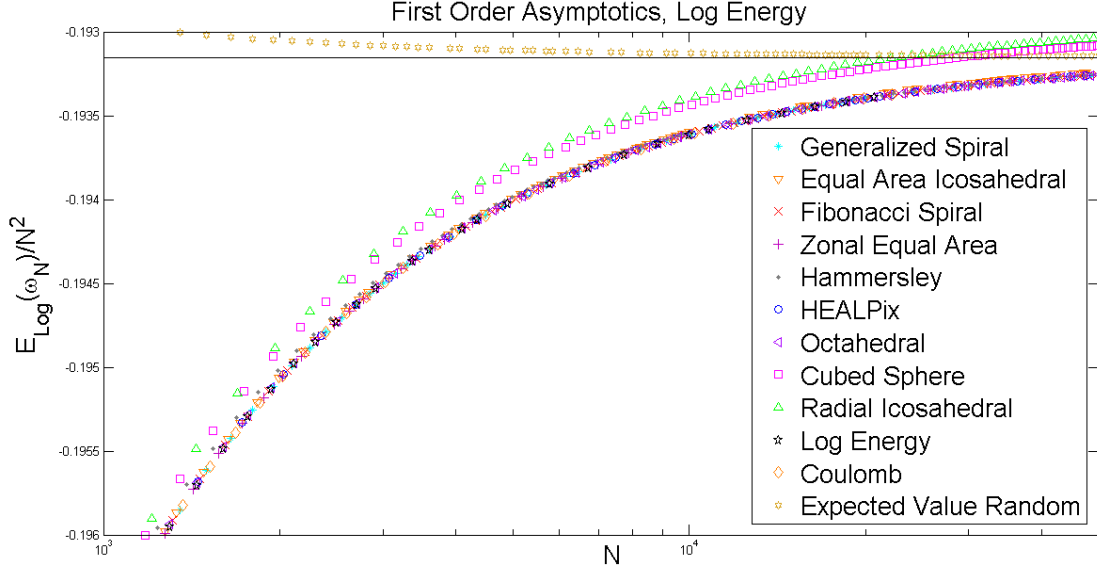


Figure 20: First order asymptotics for log potential. The solid black line is the known first order coefficient in the minimal energy expansion as given in Theorem 9.

As a corollary, Coulomb points and Fibonacci spiral points are asymptotically log optimal. We make the following natural conjecture:

Conjecture 12. *The condition on the spherical cap discrepancy in Theorem 11 can be relaxed to*

$$\lim_{N \rightarrow \infty} D(\omega_N) = 0.$$

Thus a sequence of configurations $\{\omega_N\}_{N=2}^{\infty}$ is equidistributed and well-separated iff it is asymptotically optimal with respect to logarithmic energy.

Figures 20, 21, and 22 display three comparisons of the logarithmic energies of the point sets with cardinality up to 50,000. Some configurations are sampled along subsequences to avoid overcrowding the picture. Due to the computational cost of generating approximate log energy and Coulomb points, these points are only available for $N < 22,500$. The energies of random configurations are plotted by expected value. We do not include the maximal determinant nodes because there is no known algorithm to generate them in polynomial time.

Figure 20 shows $E_{\log}(\omega_N)/N^2$ for the point sets. For the equidistributed and well-separated point sets as well as for the Hammersley nodes, this ratio converges to $1/2 - \log 2$ supporting Conjecture 12. Though the radial icosahedral and cubed sphere points are not equidistributed and thus not asymptotically optimal, their log energy appears to be of leading order N^2 .

Figure 21 displays $[E_{\log}(\omega_n) - \mathcal{I}_{\log}[\sigma]N^2]/N \log N$ for each configuration. The curves for classes of point sets begin separating. The energies of the octahedral, HEALPix, Fibonacci, generalized spiral, zonal equal area, and Coulomb points all appear to converge to the correct second order term. The energy of the Hammersley nodes appears to have $N \log N$ second term, though incorrect coefficient. While the equal area icosahedral nodes perform better than the radial icosahedral nodes, their asymptotic energy appears to have a second term

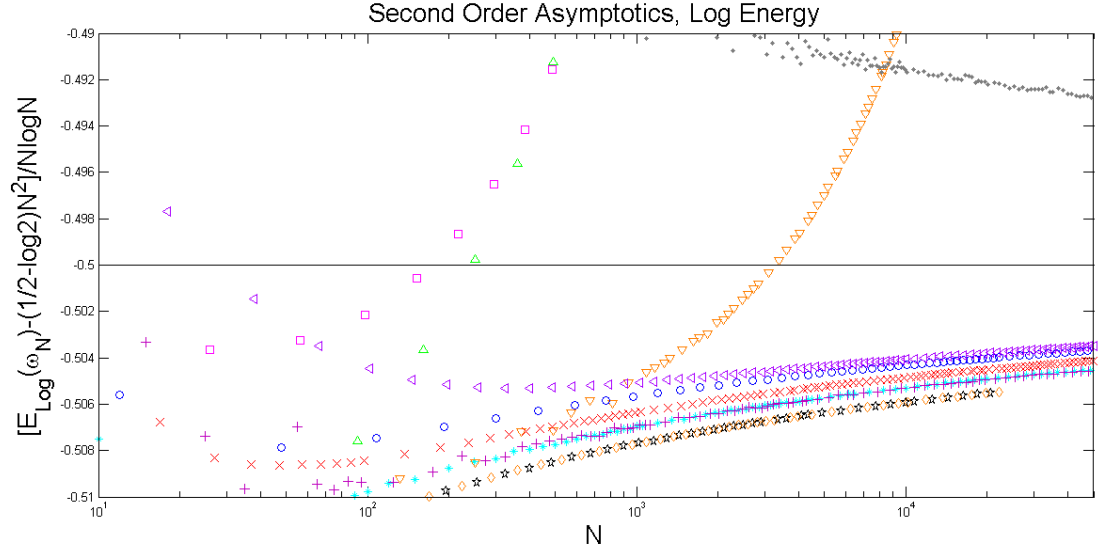


Figure 21: Second order asymptotics for log potential (with the legend of Figure 20). The solid black line corresponds to the known coefficient from Theorem 9.

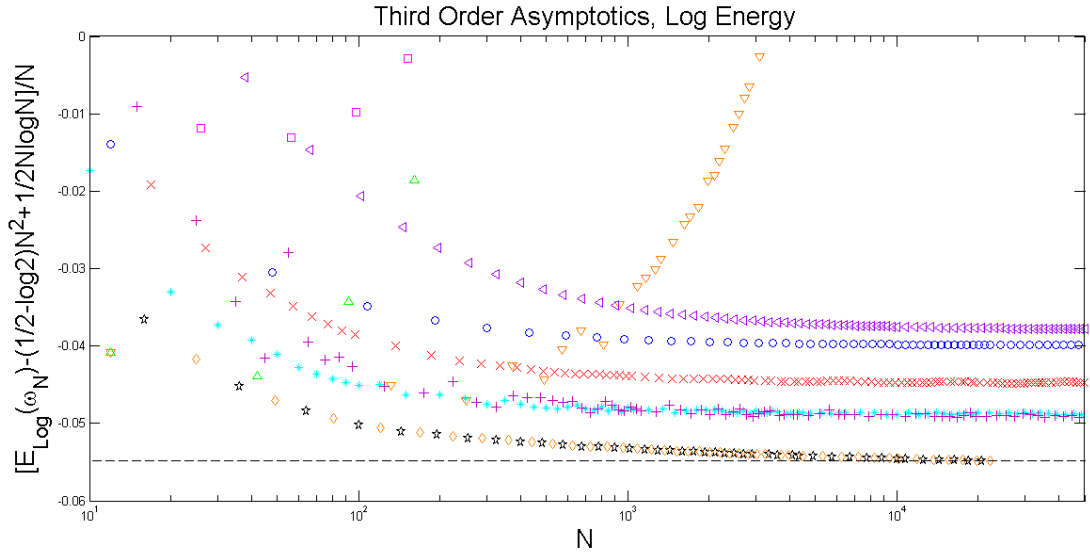


Figure 22: Third order asymptotics for log energy (with the legend of Figure 20). The dashed line is the conjectured third order constant from [17].

different to $N \log N$. Numerical second order behavior of log energy points is also studied in [44].

Figure 22 compares the energy of the configurations to the conjectured minimal log energy third order term, i.e. $[E_{\log}(\omega_n) - \mathcal{I}_{\log}[\sigma]N^2 + 1/2N \log N]/N$. Conjecture 10 is supported by the behavior of the Coulomb and log points. The octahedral, HEALPix, Fibonacci, zonal equal area, and generalized spiral configurations appear to have the third term of their energy of order N but the wrong coefficient. Of the algorithmically generated point sets, the generalized spiral and zonal equal area points perform the best with respect to the logarithmic energy.

3.2 Riesz Potential, $-2 < s < 2$, $s \neq 0$

In this range, the best known bounds on $\mathcal{E}_s(N)$ are due to Wagner (cf. [63] and [64]).

Theorem 13. *For $-2 < s < 2$, $s \neq 0$, there exist $c_s, C_s > 0$ such that for all $N \in \mathbb{N}$,*

$$c_s N^{1+s/2} \leq \mathcal{E}_s(N) - \mathcal{I}_s[\sigma]N^2 \leq C_s N^{1+s/2}.$$

Kuyljaars and Saff [34] conjecture that $\lim_{N \rightarrow \infty} [\mathcal{E}_s(N) - \mathcal{I}_s[\sigma]N^2]/N^{1+s/2}$ exists.

Conjecture 14. *For $-2 < s < 2$, $s \neq 0$,*

$$\mathcal{E}_s(N) = \mathcal{I}_s[\sigma]N^2 + \frac{(\sqrt{3}/2)^{s/2} \zeta_{\Lambda_2}(s)}{(4\pi)^{s/2}} N^{1+s/2} + o(N^{1+s/2}), \quad N \rightarrow \infty.$$

Heuristically, the second order coefficient corresponds to the Voronoi decomposition of minimal energy points being composed primarily of close to regular hexagons. A characterization of asymptotically optimal point sets is due to Leopardi [38].

Theorem 15. *If a well-separated sequence of configurations $\{\omega_N\}_{N=2}^\infty$ is equidistributed, then it is asymptotically optimal for $0 < s < 2$,*

A similar result for $s < 0$ is also known (see for example [10]).

Theorem 16. *A sequence of configurations $\{\omega_N\}_{N=2}^\infty$ is asymptotically optimal for $-2 < s < 0$ iff it is equidistributed.*

Theorems 15 and 16 are the analogs of Conjecture 12 for $-2 < s < 2$, $s \neq 0$.

In the particular case of $s = -1$, the problem of minimizing energy becomes that of maximizing sums of distances. A characterization of minimal configurations for this case is due to Stolarsky [57] (see also [15]) and is generalized by Brauchart and Dick in [14]. Let $V_t(\mathbf{z}) = \{\mathbf{x} \mid \mathbf{x} \cdot \mathbf{z} \geq t\}$ denote the spherical cap of height $1 - t$ centered at $\mathbf{z} \in \mathbb{S}^2$. The L_2 discrepancy of a configuration ω_N is defined to be

$$D_{L_2}(\omega_N) := \left(\int_{-1}^1 \int_{\mathbb{S}^2} \left(\frac{|\omega_N \cap V_t(\mathbf{z})|}{N} - \sigma(V_t(\mathbf{z})) \right)^2 d\sigma(\mathbf{z}) dt \right)^{1/2}.$$

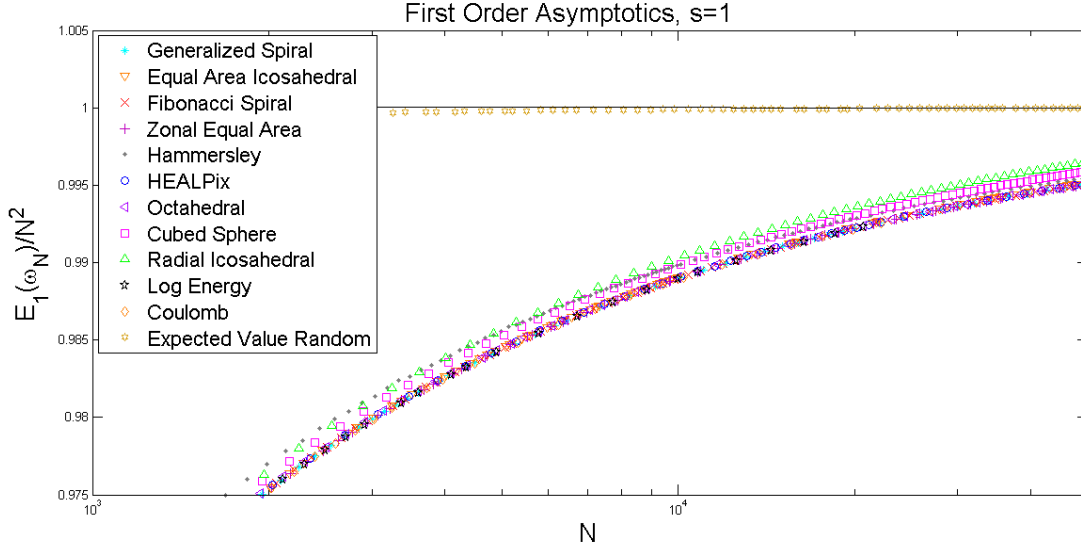


Figure 23: First order asymptotics for $s = 1$. The solid black line is the known coefficient from Theorem 13.

Theorem 17. *Stolarsky Invariance Principle.* For any $\omega_N \subset \mathbb{S}^2$,

$$\frac{1}{N^2} \sum_{i \neq j} |\mathbf{x}_i - \mathbf{x}_j| + 4D_{L_2}(\omega_N)^2 = \mathcal{I}_{-1}[\sigma] = 4/3.$$

This gives the immediate corollary (see also [13]):

Corollary 18. For a configuration ω_N , $E_{-1}(\omega_N) = \mathcal{E}_{-1}(N)$ iff ω_N minimizes L_2 discrepancy.

Figure 23 graphs the Coulomb energy of the point sets to first order. From Theorem 15, $\lim_{N \rightarrow \infty} E_1(\omega_N)/N^2 = \mathcal{I}_s[\sigma] = 1$ for all the point sets except the radial icosahedral, cubed sphere, and Hammersley nodes. As in the logarithmic case, the energies of the radial icosahedral and cubed sphere nodes appear to have N^2 leading order term but incorrect coefficient. The plot is inconclusive on whether the behavior of the Hammersley nodes is asymptotically optimal. Figure 24 shows the second order $N^{3/2}$ term from Conjecture 14. The energies of the generalized spiral, Fibonacci spiral, zonal equal area, HEALPix, and octahedral nodes all appear to converge to an $N^{3/2}$ term that is different from the conjectured value. None of these point sets have a regular hexagonal lattice structure as N gets large. Again the energies of equal area icosahedral points have a different second order term. The Hammersley nodes don't have low enough energy to appear on the plot. The asymptotic energy of the log nodes seems to have the same second order coefficient as the Coulomb nodes and both point sets support Conjecture 14. As in the logarithmic energy case, the generalized spiral and zonal equal area points perform the best of the algorithmically generated points.

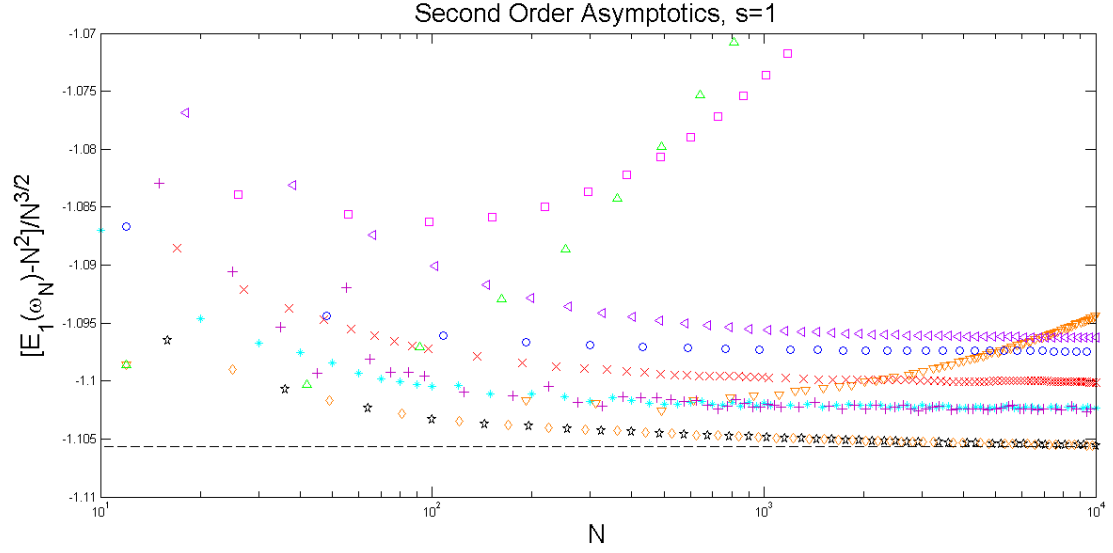


Figure 24: Second order asymptotics for $s = 1$ (with the legend of Figure 23). The dashed line is the conjectured value from [34].

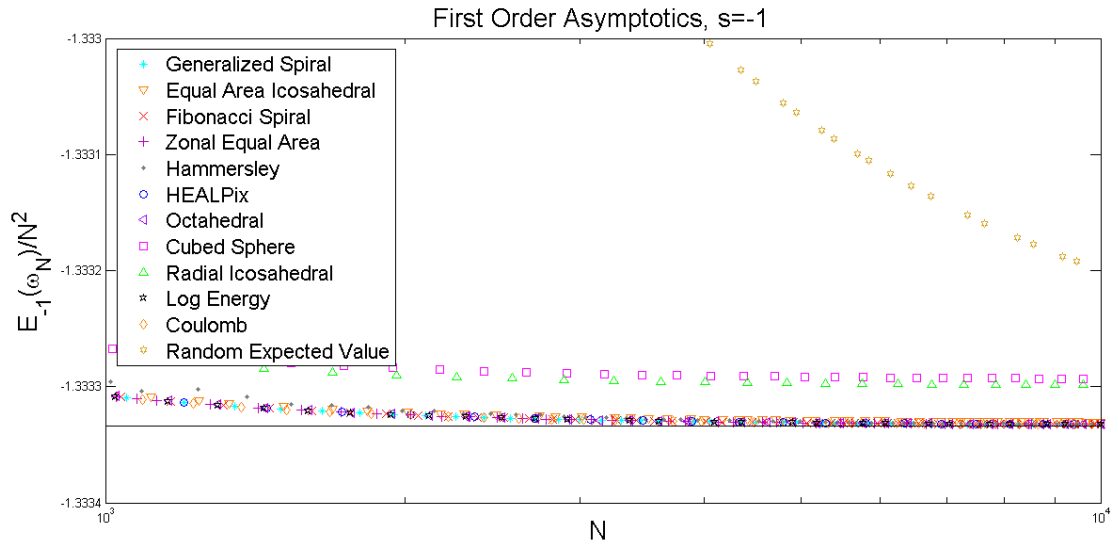


Figure 25: First order asymptotics for $s = -1$. The solid line follows from the Stolarsky invariance principle.

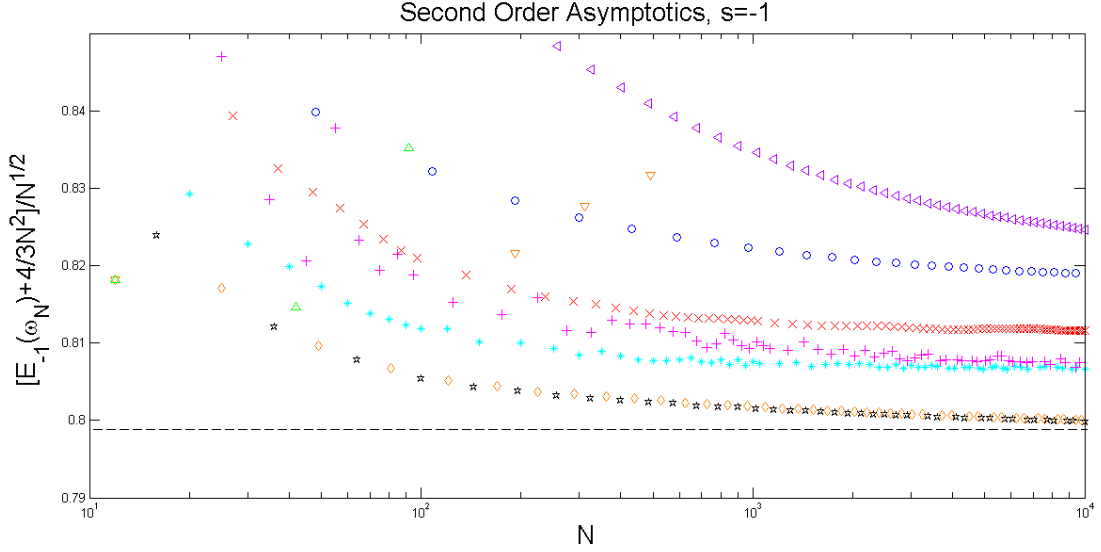


Figure 26: Second order asymptotics for $s = -1$ (with the legend of Figure 25). The dashed line is from conjecture 14.

Figure 25 displays $E_{-1}(\omega_N)/N^2$ for the point sets. Again the radial icosahedral and cubed sphere points have the correct order though they are not asymptotically optimal. For $s = -1$ The second term in the minimal energy expansion is of known order \sqrt{N} with conjectured coefficient ≈ 0.7985 . As shown in Figure 26, the behavior of the second order of the asymptotic energy of the point sets resembles that of their log and Coulomb energies. The minimal Coulomb and log energy points perform the best and support Conjecture 14. The asymptotic energies of the octahedral, HEALPix, Fibonacci, zonal equal area, and generalized spiral appear to converge to the right second order and incorrect coefficient, and the latter two configurations have the lowest energy.

3.3 Riesz Potential, $s=2$

Less is known about the case $s = 2$. The first order term was proved in [34].

Theorem 19.

$$\lim_{N \rightarrow \infty} \frac{\mathcal{E}_2(N)}{N^2 \log N} = \frac{1}{4}.$$

It is not known whether the $N^2 \log N$ term corresponds to any geometric property of the points. There is also no result analogous to Theorems 11 and 15 giving a sufficient condition for a sequence of configurations to be asymptotically optimal.

Figure 27 shows $E_2(\omega_N)/N^2 \log N$. The Hammersley points do not appear to have asymptotically minimal energy. The behavior of the octahedral, HEALPix, Fibonacci, generalized spiral, zonal equal area, and equal area icosahedral points is not clear. Their energies remain well below the known coefficient but have

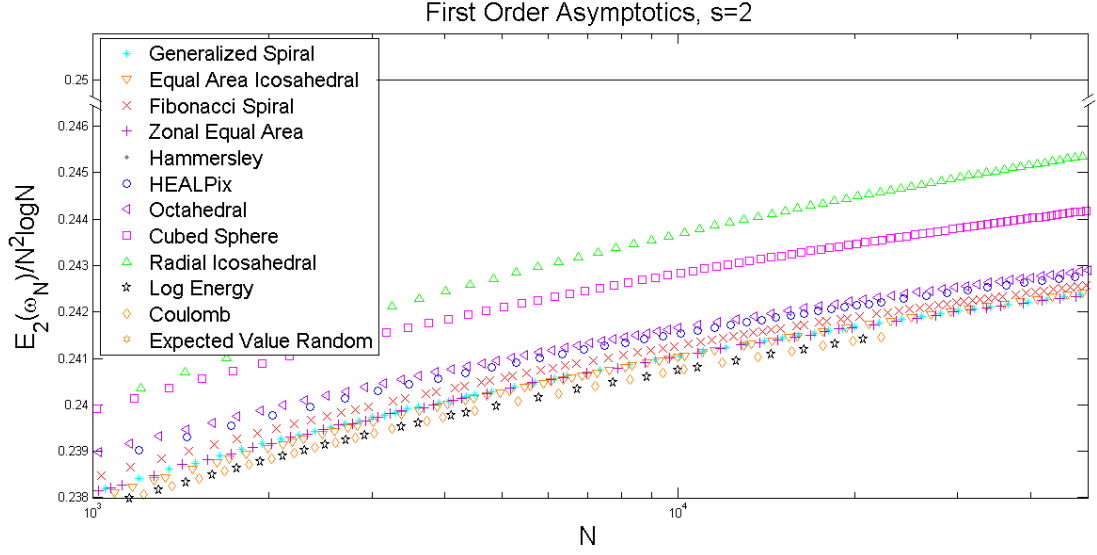


Figure 27: First order asymptotics for $s = 2$. The break in the y-axis values is to enhance the separation between the configurations. The solid line is the known coefficient from Theorem 19.

larger energy than the Coulomb and log energy points. Calculations beyond $N = 50,000$ are needed. The generalized spiral, zonal equal area, and equal area icosahedral points perform the best.

3.4 Riesz Potential, $s > 2$

In the hypersingular case $s > 2$ the continuous energy integral is infinite for any probability measure μ . Instead, the energy is known to be dominated by the nearest neighbor interactions of points as shown in a much more general result by Hardin and Saff [31].

Theorem 20. *For $s > 2$, there are constants C_s such that*

$$\lim_{N \rightarrow \infty} \frac{\mathcal{E}_s(N)}{N^{1+s/2}} = C_s, \quad 0 < C_s < \infty.$$

One can consider the analytic continuation of $\mathcal{I}_s[\sigma]$, $0 < s < 2$,

$$V_s := \frac{2^{1-s}}{2-s}, \quad s \in \mathbb{C} \setminus \{2\}.$$

The following is analogous to Conjecture 14 (see [10]).

Conjecture 21. *For $2 < s < 4$*

$$\mathcal{E}_s(N) = \frac{(\sqrt{3}/2)^{s/2} \zeta_{\Lambda_2}(s)}{(4\pi)^{s/2}} N^{1+s/2} + V_s N^2 + o(N^2).$$

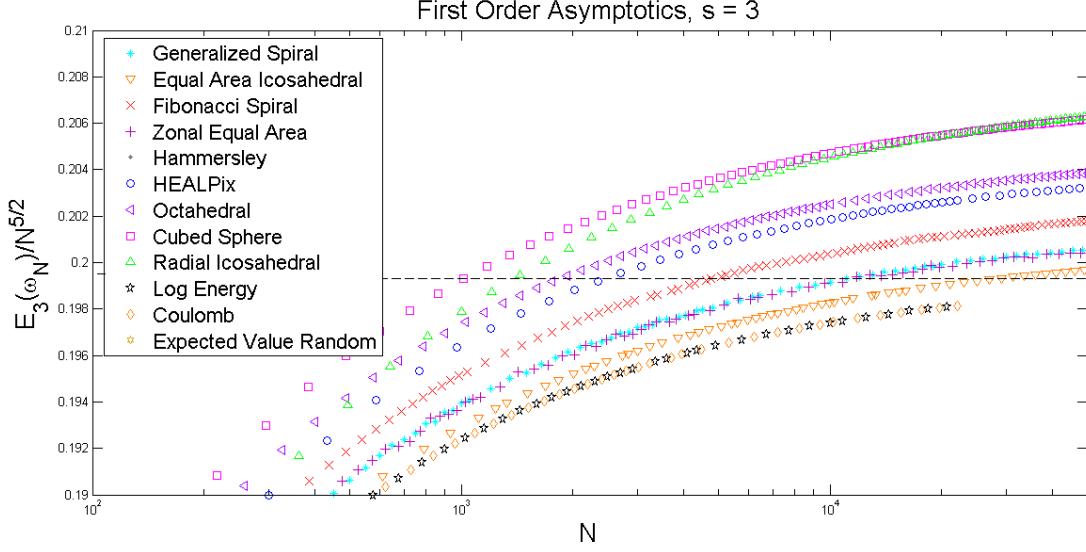


Figure 28: First order asymptotics for $s = 3$. The dashed line is the conjectured coefficient.

Figure 28 plots $E_3(\omega_N)/N^{5/2}$. The energies of most configurations seem to be going to the correct order but incorrect coefficient. The equal area icosahedral points outperform the spiral and zonal equal area points of the algorithmically generated configurations. This is expected because their Voronoi decomposition is closest to the regular hexagonal lattice. The log energy and Coulomb points again seem to be close to minimal and may converge to the conjectured $C_3 \approx 0.199522$. The Hammersley points are not seen on the plot because their asymptotic energy does not appear to have first order $N^{5/2}$.

We conclude this section with the following observation: The apparent first and second order asymptotically minimal behavior of the energy of the Coulomb and log points for the potentials we have considered is striking and we suggest a conjecture.

Conjecture 22. *The minimal logarithmic energy points and Coulomb points are asymptotically minimal to second term precision for all $-2 < s < 4$, $s \neq 0$. I.e., combined with Conjectures 14 and 21, letting $\omega_N := \omega_N^{\log}$ or ω_N^{Coul}*

$$\lim_{N \rightarrow \infty} \frac{E_s(\omega_N) - \mathcal{I}_s[\sigma]N^2}{\mathcal{E}_s(N) - \mathcal{I}_s[\sigma]N^2} = 1 \quad \text{or} \quad \lim_{N \rightarrow \infty} \frac{E_s(\omega_N) - \frac{(\sqrt{3}/2)^{s/2} \zeta_{\Lambda_2}(s)}{(4\pi)^{s/2}} N^{1+s/2}}{\mathcal{E}_s(N) - \frac{(\sqrt{3}/2)^{s/2} \zeta_{\Lambda_2}(s)}{(4\pi)^{s/2}} N^{1+s/2}} = 1.$$

Furthermore, the Coulomb points are minimal in the logarithmic energy to the third order term. That is

$$\lim_{N \rightarrow \infty} \frac{E_{\log}(\omega_N^{\text{Coul}}) - (1/2 - \log 2)N^2 + 1/2N \log N}{\mathcal{E}_{\log}(N) - (1/2 - \log 2)N^2 + 1/2N \log N} = 1.$$

4 Proofs

We begin with two auxiliary results.

Proposition 23. *Let $\{P_N\}_{N=1}^\infty$ be a diameter bounded sequence of asymptotically equal area partitions of \mathbb{S}^2 such that each P_N has N cells. For each P_N , let ω_N be a configuration of points on \mathbb{S}^2 such that the interior of each cell of P_N contains exactly one point of ω_N . Then $\{\omega_N\}_{N=1}^\infty$ is equidistributed and provides a covering of \mathbb{S}^2 with $\eta(\omega_N) \leq CN^{-1/2}$ for all $N \in \mathbb{N}$, where C is as in equation (2).*

Proof. The bound on the covering radius is trivial. Let $A \subset \mathbb{S}^2$ be a spherical cap and let

$$A_\delta := \{x \in \mathbb{S}^2 : \text{dist}(x, A) \leq \delta\},$$

where $\text{dist}(x, A) := \min_{y \in A} |x - y|$ is the standard distance function. For $x \in \omega_N$, denote by W_x^N the cell of P_N containing x . Let $\epsilon, \delta > 0$ and choose N large enough such that

$$N \min_x \sigma(W_x^N) \geq 1 - \epsilon$$

and $x \in A \cap \omega_N$ implies $W_x^N \subset A_\delta$. Then

$$\frac{|\omega_N \cap A|}{N} \leq \frac{|\{x : W_x^N \subset A_\delta\}|}{N} \leq \frac{\sigma(A_\delta)}{N \min_x \sigma(W_x^N)} \leq \frac{\sigma(A_\delta)}{1 - \epsilon}.$$

Since ϵ is arbitrary, we have

$$\limsup_N \frac{|\omega_N \cap A|}{N} \leq \sigma(A_\delta).$$

Letting $\delta \rightarrow 0$ gives

$$\limsup_N \frac{|\omega_N \cap A|}{N} \leq \sigma(A). \quad (14)$$

Applying inequality (14) to $\mathbb{S}^2 \setminus A$, we obtain

$$\liminf_N \frac{|\omega_N \cap A|}{N} = 1 - \limsup_N \frac{|\omega_N \cap (\mathbb{S}^2 \setminus A)|}{N} \geq 1 - \sigma(\mathbb{S}^2 \setminus A) = \sigma(A),$$

and thus, we have

$$\lim_{N \rightarrow \infty} \frac{|\omega_N \cap A|}{N} = \sigma(A).$$

□

Proof of Theorem 1.

For a fixed N denote in spherical coordinates $x_i := (\phi_i, \theta_i) \in \omega_N$. We first prove the separation bound. Let $\epsilon_N = 2\sqrt{4\pi/N}$. For large N , by the pigeonhole principle, at least one set of adjacent points $x_k, x_{k+1} \in \omega_N$ is separated along S_N by a distance less than $\sqrt{4\pi/N}$. So we can restrict our attention to $k \leq N/2$ and ϵ_N -balls $B(x_k, \epsilon_N)$. For large N , if $k < 8\pi + 1/2$, then

$$\cos \phi_k = 1 - \frac{2k-1}{N} \geq 1 - \frac{16\pi}{N} \approx \cos(2\sqrt{\frac{4\pi}{N}}),$$

and x_k is within the first two full longitudinal turns of S_N starting from a pole. Otherwise, $B(x_k, \epsilon_N)$ contains disjoint levels of S_N . In this case, the minimal distance between levels in $B(x_k, \epsilon_N)$ is $\sqrt{4\pi/N}$. We compute the nearest neighbor distance between points in the same level as follows. Let

$$f_N(k) := \sqrt{N}|x_k - x_{k+1}|, \quad x_k \in \omega_N, \quad k < N/2.$$

Using the distance formula for spherical coordinates

$$|x_j - x_k|^2 = 2 - 2(\cos \phi_j \cos \phi_k + \sin \phi_j \sin \phi_k \cos(\theta_j - \theta_k)) \quad (15)$$

and expanding $\cos^{-1} x$ around $x = 1$ we have

$$\lim_{N \rightarrow \infty} f_N(k) = \sqrt{8k - 4\sqrt{4k^2 - 1} \cos(\sqrt{2\pi}(\sqrt{2k-1} - \sqrt{2k+1}))}, \quad (16)$$

and $f_N(k) < f_{N+1}(k)$ for all $k < N/2 - 1$ and large N . Thus we have the correct order for the minimal separation between adjacent points in ω_N . Furthermore, (16) is increasing as a function of k and thus

$$\lim_{N \rightarrow \infty} \min_k f_N(k) = \sqrt{8 - 4\sqrt{3} \cos(\sqrt{2\pi}(1 - \sqrt{3}))}. \quad (17)$$

Lastly, around the north pole, $k_1, k_2 < 8\pi + 1/2$, we can again use (15) to show that

$$\lim_{N \rightarrow \infty} \sqrt{N}|x_{k_1} - x_{k_2}|$$

exists and can be computed case by case for pairs (k_1, k_2) . The southern hemisphere can be similarly computed. Comparing to (17) gives the separation constant (5).

For covering, given $y \in \mathbb{S}^2$,

$$\text{dist}(S_N) \leq \sqrt{\frac{\pi}{N}}.$$

From (16), the maximal distance from any point on S_N to a point of ω_N is $O(1/\sqrt{N})$ and thus the covering radius of ω_N is also $O(1/\sqrt{N})$.

We have two additional observations. First, the Voronoi decompositions of the spiral points are diameter bounded. Secondly, the Voronoi cells are asymptotically equal area on $K_h := \{(x, y, z) \in \mathbb{S}^2 : -h \leq z \leq h\}$ for any fixed $0 < h < 1$. By this we mean

$$\lim_{N \rightarrow \infty} N \max_{V_x(\omega_N) \subset K_h} \sigma(V_x(\omega_N)) = \lim_{N \rightarrow \infty} N \min_{V_x(\omega_N) \subset K_h} \sigma(V_x(\omega_N)) = 1.$$

Indeed, fixing h , for any $\epsilon > 0$, we can take N large enough such that given $x_i = (\phi_i, \theta_i) \in K_h \cap \omega_N$, x_{i-1} , and x_{i+1} are almost iso-latitudinal with x_i with separation $\sqrt{4\pi/N}$. I.e.,

$$|x_{i\pm 1} - (\phi_i, \theta_i \pm \csc \phi_i \sqrt{4\pi/N})| < \epsilon.$$

There exists shifts $0 \leq \lambda_{i+}, \lambda_{i-} \leq \sqrt{4\pi/N}$ such that the nearest points in the adjacent spiral levels are within ϵ of the points $(\phi_i \pm \sqrt{4\pi/N}, \theta_i + \csc \phi_i \lambda_{i\pm})$

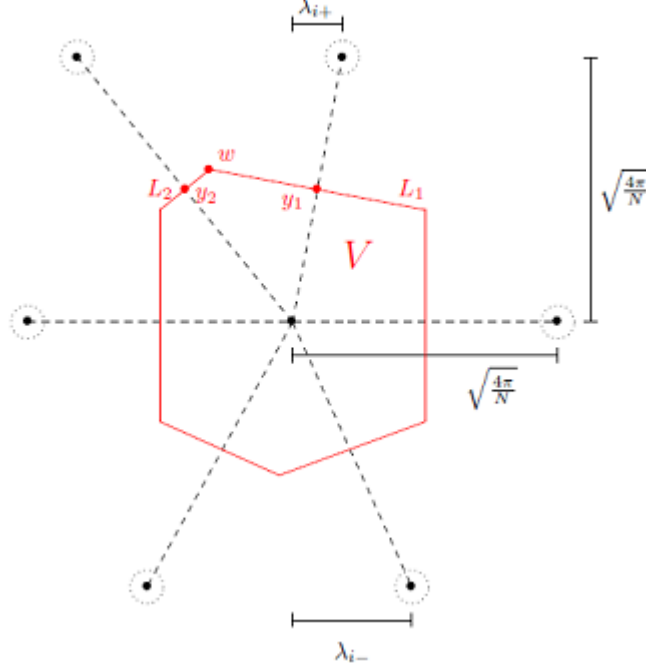


Figure 29: Limiting form of Voronoi cell for each $x_i \in K_h \cap \omega_N$ with relevant quantities labeled. We can choose N large enough such that the nearest neighbors of x_i lie within ϵ of the points taken along iso-latitudinal lines separated by $\sqrt{4\pi/N}$

and $(\phi_i \pm \sqrt{4\pi/N}, \theta_i + \csc \phi_i(\lambda_{i\pm} - \sqrt{4\pi/N}))$. Thus as $N \rightarrow \infty$, the Voronoi cell $V_i(\omega_N)$ approaches the form of V in Figure 29 and

$$\sigma(V_i(\omega_N)) = \sigma(V) + O(\epsilon^2).$$

Furthermore, we can treat V as a planar polygon in Figure 29, and

$$\sigma(V) = \frac{1}{N}$$

independent of the shifts $\lambda_{i\pm}$. This we show by direct computation.

Letting $a = \sqrt{4\pi/N}$ and centering x_i at $(0,0)$, the points $y_1 = (\lambda_{i+}/2, a/2)$ and $y_2 = ((\lambda_{i+} - a)/2, a/2)$ are the midpoints of the lines connecting x_i to its nearest neighbors in the adjacent level which are shifted by λ_{i+} . The corresponding lines

$$L_1 : y = -\frac{\lambda_{i+}}{a}(x - \frac{\lambda_{i+}}{2}) + \frac{a}{2} \quad L_2 : y = \frac{a - \lambda_{i+}}{a}(x - \frac{\lambda_{i+} - a}{2}) + \frac{a}{2}$$

form the top boundary of V and have intersection point

$$w := (\lambda_{i+} - a/2, (\lambda_{i+}a + a^2 - \lambda_{i+}^2)/2a).$$

From this we calculate the area of the top half of V to be

$$\sigma(V_{top}) = \frac{1}{4\pi} \left[a \left(\frac{-a\lambda_{i+} + \lambda_{i+}^2 + a^2}{2a} \right) + \frac{a}{2} \left(\frac{a\lambda_{i+} - \lambda_{i+}^2}{a} \right) \right] = \frac{1}{2N}.$$

The same calculation holds for the bottom half of V and thus (3) holds.

We now consider equidistribution. Because the height steps between points in ω_N are uniform, for a spherical cap A centered at a pole,

$$\lim_{N \rightarrow \infty} \frac{|\omega_N \cap A|}{N} = \sigma(A). \quad (18)$$

If A does not contain one of the poles, then $A \subset K_h$ for some h and (18) holds by Proposition 23. Finally if A is a cap containing but not centered at one of the poles, A can be partitioned into an open cap of height h centered at the pole and $A \cap K_h$. Because (18) holds on each disjoint subset, it also holds on A . \square

Proof of Proposition 2.

When $z = k$, the basis vector $\mathbf{c}_{k,i}$ has minimum length of $\sqrt{2}d$. At this latitude, $\mathbf{c}_{k+1,i}$ and $\mathbf{c}_{k-1,i}$ form the next most dominant spirals and have length $\sqrt{3}d$. For $z = k + 1/2$, $\mathbf{c}_{k,i}$ and $\mathbf{c}_{k+1,i}$ are equally dominant and have grid length $\sqrt[4]{5}d$. For a fixed latitude $\phi \neq \pm\pi/2$, z increases with N . Points around ϕ will form a locally rectangular grid. Thus the separation approaches $\sqrt{2}d$ which occurs when $z = k$ and the largest hole in the triangulation around x_i will be at most $\sqrt[4]{5}d/\sqrt{2}$ which occurs when $z = k \pm 1/2$. Thus off the poles, $\delta(\omega_{2N+1}) \geq \sqrt{8\pi\sqrt{5}}/\sqrt{N}$ and $\eta(\omega_{2N+1}) \leq \sqrt{2\pi/N}$.

Indeed, these inequalities hold for large zone numbers z where $F_k \approx \varphi^k/\sqrt{5}$ holds. However, on the polar points, x_1 and x_N , the zone number

$$z = \frac{\log((2N+1)\pi\sqrt{5}(1-4N^2/(2N+1)^2))}{\log \varphi^2} \rightarrow \frac{\log(2\pi\sqrt{5})}{\log \varphi^2} = 2.75\dots, \quad N \rightarrow \infty$$

and writing $\mathbf{c}_{k,i}$ in the form of equation (8) for small k overestimates the length of the vector. Using equation (7) and noticing that $k - 1/2 \leq z \leq k + 1/2$ implies

$$\frac{\varphi^{2k-1}}{(2N+1)\pi\sqrt{5}} \leq \cos^2 \phi \leq \frac{\varphi^{2k+1}}{(2N+1)\pi\sqrt{5}},$$

we have

$$|\mathbf{c}_{k,i}|^2 \geq \frac{4\pi^2\varphi + 20\pi F_k^2\varphi^{-2k+1}}{(2N+1)\pi\sqrt{5}} = O\left(\frac{1}{2N+1}\right), \quad k - 1/2 \leq z \leq k + 1/2.$$

Since $|\mathbf{c}_{k,i}|$ is the minimal separation distance for $k - 1/2 \leq z \leq k + 1/2$, we have the correct order of separation on \mathbb{S}^2 . By a similar computation, we have the upper bound

$$|\mathbf{c}_{k,i}| \leq O\left(\frac{1}{\sqrt{2N+1}}\right), \quad k - 3/2 \leq z \leq k + 3/2.$$

Since the triangulation of ω_{2N+1} in each zone consists of $\mathbf{c}_{k,i}$, $\mathbf{c}_{k-1,i}$, and $\mathbf{c}_{k+1,i}$, the covering of ω_{2N+1} is of the correct order on all of \mathbb{S}^2 . \square

Proof of Proposition 3.

The diameter boundedness of the partition and Proposition 23 gives equidistribution and covering,

$$\eta(\omega_N) \leq \frac{3.5}{\sqrt{N}}.$$

In [37] and [67], it is established that there exists $c_1, c_2 > 0$ such that for all partitions P_N , with ϕ_j , n as defined above,

$$\frac{c_1}{\sqrt{N}} \leq \phi_{j+1} - \phi_j \leq \frac{c_2}{\sqrt{N}}, \quad 0 \leq j \leq n. \quad (19)$$

This gives the correct order of separation between collars. For neighbors $x_1, x_2 \in \omega_N$ within collar j , wlog suppose $\phi_j < \pi/2$. Using the fact that the normalized area of each cell can be expressed as

$$\frac{(\cos \phi_j - \cos \phi_{j+1})}{2y_i} = \frac{1}{N},$$

we have

$$|x_1 - x_2| \geq \frac{2\pi \sin \phi_j}{y_i} = \frac{4\pi \sin \phi_j}{N(\cos \phi_j - \cos \phi_{j+1})}.$$

So it suffices to show there exists $c_3 > 0$ such that

$$\frac{\sin \phi_j}{\cos \phi_j - \cos \phi_{j+1}} \geq c_3 \sqrt{N} \quad \forall N, 0 \leq j \leq n. \quad (20)$$

For a fixed $h > 0$ and $\phi_j \geq h$, this follows from (19) and the fact that \cos is Lipschitz. On the other hand, for sufficiently small ϕ_j , there exists $c_4 > 0$ such that

$$\frac{\sin \phi_j}{\cos \phi_j - \cos \phi_{j+1}} \geq c_4 \frac{\phi_j}{\phi_j^2 - \phi_{j+1}^2}.$$

Again applying (19) twice,

$$\text{RHS (20)} \geq \frac{c_4}{c_1} \frac{\phi_j}{\phi_j + \phi_{j+1}} \sqrt{N} \geq \frac{c_4}{c_1} \frac{\phi_j}{2\phi_j + \frac{c_2}{\sqrt{N}}} \sqrt{N} \geq c_3 \sqrt{N}.$$

In the last step we used the fact that for some $c_5 > 0$ and all j

$$\phi_j \geq \cos^{-1}\left(1 - \frac{2}{N}\right) \geq \frac{c_5}{\sqrt{N}}.$$

□

Proof of Proposition 4.

The pixels are diameter bounded and thus by Proposition 23 the nodes are equidistributed.

To establish separation, we examine the five cases of nearest neighbor points: The points lie in 1) the polar region or 2) the equatorial region, and the points lie in a) the same ring or b) adjacent rings, and 3) the points lie in adjacent rings at the boundary of the polar region and the equatorial region.

Case 1a: If nearest neighbor points lie in the polar region along the same ring $1 \leq i \leq k$ that has radius

$$r_i = \sin \phi_i = \sqrt{\frac{2i^2}{3k^2} - \frac{i^4}{9k^4}}$$

and $4i$ equally spaced points, then the separation δ satisfies

$$\delta = 2r_i \sin \frac{\pi}{4i} = 2\sqrt{\frac{2i^2}{3k^2} - \frac{i^4}{9k^4}} \sin \frac{\pi}{4i} \geq \frac{\sqrt{2}}{i} \sqrt{\frac{2i^2}{3k^2} - \frac{i^4}{9k^4}} = O\left(\frac{1}{k}\right) = O\left(\frac{1}{\sqrt{N}}\right).$$

In the middle inequality we use the fact that

$$\sin x \geq \frac{\sqrt{2}/2}{\pi/4} x \quad 0 \leq x \leq \pi/4. \quad (21)$$

Case 2a: Suppose the nearest neighbor points lie in the equatorial region along the same ring. Since each ring has $4k$ points, the smallest separation occurs at the ring farthest from the equator and closest to $z = 2/3$. Using (21) again, we have

$$\delta = 2r_i \sin \frac{\pi}{4k} \geq \frac{2\sqrt{5}}{3} \sin \frac{\pi}{4k} \geq \frac{\sqrt{10}}{3k} = O\left(\frac{1}{\sqrt{N}}\right).$$

Case 1b: We split up the rings in the polar region into the outer half, $1 \leq i \leq k/2$ and the inner half, $k/2 \leq i \leq k$. On the outer half, the separation between rings is

$$\begin{aligned} \delta \geq r_{i+1} - r_i &= \frac{(i+1)\sqrt{6k^2 - (i+1)^2} - i\sqrt{6k^2 - i^2}}{3k^2} \\ &\geq \frac{(k/2+1)\sqrt{6k^2 - (k/2+1)^2} - (k/2)\sqrt{6k^2 - (k/2)^2}}{3k^2} = O\left(\frac{1}{\sqrt{N}}\right). \end{aligned}$$

On the inner polar rings, the separation between rings is

$$\delta \geq |\cos \phi_{i+1} - \cos \phi_i| = \frac{2i+1}{3k^2} \geq \frac{k+1}{3k^2} = O\left(\frac{1}{\sqrt{N}}\right).$$

Case 2b: In the equatorial region, the ring height z increases linearly with respect to the index i giving

$$\delta \geq \frac{2}{3k} = O\left(\frac{1}{\sqrt{N}}\right).$$

Case 3 follows from Case 1b and 2b.

The covering of the points follows by similar geometric arguments. \square

Proof of Proposition 5.

It suffices to show Π is locally bi-Lipschitz on each face \mathcal{F} of the icosahedron. If for some $\delta, L_1, L_2 > 0$

$$L_1|x - y| \leq |\Pi(x) - \Pi(y)| \leq L_2|x - y|, \quad x, y \in \mathcal{F}, \quad |x - y| < \delta,$$

then

$$\gamma(\omega_N) \leq \frac{L_2}{L_1} \gamma(\widetilde{\omega_{N_k}}) = \frac{L_2}{L_1 \sqrt{3}}.$$

Let $c := \min_{x \in \text{Icos}} |x| = \sqrt{(1/3 + 2\sqrt{5}/15)}$. For $x, y \in \mathcal{F}$ with angle θ , we have

$$|x - y| \geq 2c \sin \frac{\theta}{2}.$$

Using the fact that $\sin^{-1} x \leq \frac{\pi}{2} x$ for $x \leq 1$ and $|x - y| < 2c$,

$$|\Pi(x) - \Pi(y)| \leq \theta \leq 2 \sin^{-1} \left(\frac{|x - y|}{2c} \right) \leq \pi c |x - y|.$$

For the other inequality, wlog suppose $c \leq |x| \leq |y| \leq 1$, and consider the line $P \subset \mathcal{F}$ connecting x and y . Denote z as the projection of 0 onto P . Defining $\phi := \cos^{-1}(|z|/|x|)$, we have

$$|y| - |x| = |z| \sec(\theta + \phi) - |z| \sec \phi \leq \sec(\theta + \phi) - \sec \phi.$$

Since $\phi \leq \cos^{-1} c - \theta$ and secant is convex on $(0, \pi/2)$,

$$|y| - |x| \leq \frac{1}{c} - \sec(\cos^{-1} c - \theta) =: g(\theta).$$

Thus,

$$\begin{aligned} |x - y|^2 &= |x|^2 + |y|^2 - 2|x||y| \cos \theta \leq \max_{c \leq |y| \leq 1} (|y| + g)^2 + |y|^2 - 2|y|(|y| + g) \cos \theta \\ &= (1 + g)^2 + 1 - 2(1 + g) \cos \theta. \end{aligned}$$

Since

$$f(\theta) := \frac{(1 + g)^2 + 1 - 2(1 + g) \cos \theta}{2 - 2 \cos \theta}$$

is continuous for $\theta \in (0, \pi/2 + \cos^{-1} c)$ and $\lim_{\theta \rightarrow 0} f(\theta)$ exists, there exists $L > 0$ such that

$$|x - y| \leq L |\Pi(x) - \Pi(y)|, \quad \theta \in (0, \pi/2 + \cos^{-1} c).$$

□

Proof of Theorem 6. Restricting ourselves to the face of \mathbb{K} with all positive coordinates, label the vertices of the partition $\{A_{i,j}\}_{0 \leq i+j \leq k}$ by

$$A_{i,j} = \left(\frac{iL}{k\sqrt{2}}, \frac{jL}{k\sqrt{2}}, \frac{L}{\sqrt{2}} \left(1 - \frac{i+j}{k} \right) \right).$$

Let $\mathcal{A}_{i,j} = \mathcal{U}(A_{i,j})$. Then

$$\mathcal{A}_{i,j} = \left(\frac{i+j}{k} \sqrt{2 - \frac{(i+j)^2}{k^2}} \cos \frac{\pi j}{2(i+j)}, \frac{i+j}{k} \sqrt{2 - \frac{(i+j)^2}{k^2}} \sin \frac{\pi j}{2(i+j)}, 1 - \frac{(i+j)^2}{k^2} \right).$$

Then

$$\delta(\omega_N) = \min_{i,j} \{ \|\mathcal{A}_{i+1,j} - \mathcal{A}_{i,j}\|, \|\mathcal{A}_{i,j+1} - \mathcal{A}_{i,j}\|, \|\mathcal{A}_{i+1,j} - \mathcal{A}_{i,j+1}\| \}. \quad (22)$$

Adapting [33], we have

$$\begin{aligned}\|\mathcal{A}_{i+1,j} - \mathcal{A}_{i,j}\|^2 &= 2\frac{(i+j+1)^2}{k^2} + 2\frac{(i+j)^2}{k^2} - 2\frac{(i+j+1)^2(i+j)^2}{k^4} \\ &\quad - 2\frac{(i+j)(i+j+1)}{k^2}\sqrt{2 - \frac{(i+j+1)^2}{k^2}}\sqrt{2 - \frac{(i+j)^2}{k^2}}\cos\frac{\pi j}{2(i+j)(i+j+1)}.\end{aligned}$$

Along the line $i+j = c$, the minimum is obtained when the cosine term is maximized, i.e. at $j = 0$. Thus

$$\begin{aligned}\min_{i,j} \|\mathcal{A}_{i+1,j} - \mathcal{A}_{i,j}\|^2 &= \min_{0 \leq i \leq k} \|\mathcal{A}_{i+1,0} - \mathcal{A}_{i,0}\|^2 \\ &= \frac{2}{k^2} \min_{0 \leq i \leq k} \left((i+1)^2 + i^2 + \frac{(i+1)^2 i^2}{k^2} - i(i+1)\sqrt{2 - \frac{(i+1)^2}{k^2}}\sqrt{2 - \frac{i^2}{k^2}} \right) = \frac{2}{k^2}.\end{aligned}$$

By symmetry of the above expressions in i and j ,

$$\min_{i,j} \|\mathcal{A}_{i,j+1} - \mathcal{A}_{i,j}\|^2 = \min_{0 \leq j \leq k} \|\mathcal{A}_{0,j+1} - \mathcal{A}_{0,j}\|^2 = \frac{2}{k^2}.$$

Lastly,

$$\|\mathcal{A}_{i+1,j} - \mathcal{A}_{i,j+1}\|^2 = 4\frac{(i+j+1)^2}{k^2} \left(2 - \frac{(i+j+1)^2}{k^2} \right) \sin^2 \frac{\pi}{4(i+j+1)}$$

which again depends on only $i+j$. Using (21) we have

$$\begin{aligned}\min_{i,j} \|\mathcal{A}_{i+1,j} - \mathcal{A}_{i,j+1}\|^2 &= \min_{0 \leq i \leq k} \|\mathcal{A}_{i+1,0} - \mathcal{A}_{i,1}\|^2 \\ &= 4 \min_{0 \leq i \leq k} \frac{(i+1)^2}{k^2} \left(2 - \frac{(i+1)^2}{k^2} \right) \sin^2 \frac{\pi}{4(i+1)} \\ &\geq 4 \min_{0 \leq i \leq k} \frac{(i+1)^2}{k^2} \left(2 - \frac{(i+1)^2}{k^2} \right) \frac{1}{2(i+1)^2} \\ &= 4 \min_{0 \leq i \leq k} \frac{1}{2k^2} \left(2 - \frac{(i+1)^2}{k^2} \right) = \frac{2}{k^2} \left(2 - \frac{(k+1)^2}{k^2} \right).\end{aligned}$$

Thus from (22)

$$\delta(\omega_{4k^2+2})^2 \geq \frac{2}{k^2} \left(2 - \frac{(k+1)^2}{k^2} \right).$$

Taking the square root and substituting $N = 4k^2 + 2$ gives

$$\liminf_{N \rightarrow \infty} \delta(\omega_N) \sqrt{N} \geq \sqrt{8}.$$

Finally, the diameter bound in [33] gives an immediate upper bound for the covering radius from which (11) follows:

$$\eta(\omega_{4k^2+2}, \mathbb{S}^2) \leq \sqrt{\frac{4 + \pi^2}{8k^2}}.$$

□

5 Matlab Code

Many thanks to Grady Wright for his help in implementing some of these point sets in Matlab. Code for the Fibonacci, Hammersley, HEALPix, and cubed sphere nodes authored by Wright is available at <https://github.com/gradywright/spherepts>. The approximate Coulomb, log energy, and maximum determinant points were provided from computations by Rob Womersley. Code for the zonal equal area points is available in Paul Leopardi's Recursive Zonal Equal Area Toolbox from eqsp.sourceforge.net. Code for the generalized spiral, octahedral, radial icosahedral, and equal area icosahedral nodes was created by the authors and is available upon request.

6 References

- [1] C. Aistleitner, J.S. Brauchart, and J. Dick. Point sets on the sphere \mathbb{S}^2 with small spherical cap discrepancy. *Discrete Comput. Geom.*, 48(4):990–1024, 2012.
- [2] R. Bauer. Distribution of points on a sphere with application to star catalogs. *J. Guid. Cont. Dyn.*, 23(1):130–137, 2000.
- [3] J. Beck. Sums of distances between points on a spherean application of the theory of irregularities of distribution to discrete geometry. *Mathematika*, 31(1):33–41, 1984.
- [4] C. Beltran. A facility location formulation for stable polynomials and elliptic Fekete points. *Found. Comput. Math.*, 15:125–157, 2015.
- [5] R. Berman, S. Boucksom, and D. Nystrom. Fekete points and convergence towards equilibrium measures on complex manifolds. *Acta Math.*, 207(1):1–27, 2011.
- [6] L. Bétermin and E. Sandier. Renormalized energy and asymptotic expansion of optimal logarithmic energy on the sphere. To appear, ArXiv preprint: <http://arxiv.org/abs/1404.4485>.
- [7] D. Bilyk, V.N. Temlyakov, and R. Yu. Fibonacci sets and symmetrization in discrepancy theory. *J. Complexity*, 28(1):18–36, 2013.
- [8] A. Bondarenko, D. Radchenko, and M. Viazovska. Well separated spherical designs. *Constructive Approximation*, 41(1):93–112, 2014.
- [9] A.V. Bondarenko, D.P. Hardin, and E.B. Saff. Mesh ratios for best-packing and limits of minimal energy configurations. *Acta Math. Hungar.*, 142(1):118–131, 2012.
- [10] S.V. Boradachov, D.P. Hardin, and E.B. Saff. *Minimal discrete energy on rectifiable sets*. Springer, to appear.
- [11] M.J. Bowick, A. Cacciuto, D.R. Nelson, and A. Travesset. Crystalline order on a sphere and the generalized Thompson problem. *Phys. Rev. Lett.*, 89, 2002.

- [12] M.J. Bowick and L. Giomi. Two-dimensional matter: Order, curvature and defects. *Adv. Phys.*, 58:449–563, 2009.
- [13] J.S. Brauchart. Optimal discrete Riesz energy and discrepancy. *Unif. Distrib. Theory*, 6(2):207–220, 2011.
- [14] J.S. Brauchart and J. Dick. A characterization of Sobolev spaces on the sphere and an extension of Stolarsky’s invariance principle to arbitrary smoothness. *Constr. Approx.*, 3:1–49, 2013.
- [15] J.S. Brauchart and J. Dick. A simple proof of Stolarsky’s invariance principle. *Proc. Amer. Math. Soc.*, 141(6):2085–2096, 2013.
- [16] J.S. Brauchart, J. Dick, and L. Fang. Spatial low discrepancy sequences, spherical cone discrepancy, and applications in financial modeling. *J. Comput. Appl. Math.*, 286:28–53, 2015.
- [17] J.S. Brauchart, D.P. Hardin, and E.B. Saff. The next-order term for minimal Riesz and logarithmic energy asymptotics on the sphere. *Contemp. Math.*, 578:31–61, 2012.
- [18] J.S. Brauchart, E.B. Saff, I.H. Sloan, Y.G. Wang, and R.S. Womersley. Random point sets on the sphere – hole radii, covering, and separation. submitted.
- [19] J.S. Brauchart, E.B. Saff, I.H. Sloan, and R.S. Womersley. QMC designs: Optimal order quasi-monte carlo integration schemes on the sphere. *Math. Comput.*, 83(290):2821–2851, 2014.
- [20] M. Calef. *Theoretical and computational investigations of minimal energy problems*. PhD thesis, Vanderbilt University, 2009.
- [21] D.L.D. Caspar and A. Klug. Physical principles in the construction of regular viruses. *Cold Springs Harb. Symp. Quant. Biol.*, 27, 1962.
- [22] H.S.M Coxeter. The role of intermediate convergents in Tait’s explanation for phyllotaxis. *J Algebra*, 20:167–175, 1972.
- [23] J. Cui and W. Freeden. Equidistribution on the sphere. *SIAM J. Sci. Comput.*, 18(2):595–609, 1997.
- [24] B. Dahlberg. On the distribution of Fekete points. *Duke Math. J.*, 45(3):537–542, 1978.
- [25] R. Dixon. Spiral phyllotaxis. *Comput. Math. Appl.*, 17:535–538, 1992.
- [26] P.D. Dragnev. On the separation of logarithmic points on the sphere. In *Approx. Theory X*, pages 137–144. Vanderbilt University Press, Nashville, TN, 2002.
- [27] E.J. Fuselier and G.B. Wright. Stability and error estimates for vector field interpolation and decomposition on the sphere with rbfs. *SIAM J. Numer. Anal.*, 47(5):3213–39, 2009.

- [28] F.X. Giraldo, J.S. Hesthave, and T. Warburton. Nodal high-order discontinuous galerkin methods for the spherical shallow water equations. *J. Comput. Phys.*, 181(2):499–525, 2002.
- [29] M. Goldberg. A class of multi-symmetric polyhedron. *Tohoku Math. J.*, 43:104–108, 1937.
- [30] K.M. Gorski, E. Hivon, A.J. Banday, B.D. Wandelt, F.K. Hansen, M. Reinecke, and M. Bartelman. HEALPix-a framework for high resolution discretization, and fast analysis of data distributed on the sphere. *Astrophys. J.*, 622:759–771, 2005.
- [31] D.P. Hardin and E.B. Saff. Minimal Riesz energy point configurations for rectifiable d -dimensional manifolds. *Adv. Math.*, 193:174–204, 2005.
- [32] A. Holhoş and D. Roşca. Area preserving maps and volume preserving maps between a class of polyhedrons and a sphere. ArXiv preprint: <http://arxiv.org/abs/1504.01517>.
- [33] A. Holhoş and D. Roşca. An octahedral equal area partition of the sphere and near optimal configurations of points. *Comput. Math. Appl.*, 67:1092–1107, 2014.
- [34] A.B.J. Kuijlaars and E.B. Saff. Asymptotics for minimal discrete energy on the sphere. *Trans. Amer. Math. Soc.*, 350(2):523–538, 1998.
- [35] L. Kuipers and H. Niederreiter. *Uniform distribution of sequences*. Wiley-Interscience, New York, 1974.
- [36] P. Leopardi. A partition of the unit sphere into regions of equal area and small diameter. *Electron. Trans. on Numer. Anal.*, 25:309–327, 2006.
- [37] P. Leopardi. Diameter bounds for equal area partitions of the unit sphere. *Electron. Trans. Numer. Anal.*, 35:1–16, 2009.
- [38] P. Leopardi. Discrepancy, separation, and Riesz energy of finite point sets on the unit sphere. *Adv. Comput. Math.*, 39(1):27–43, 2013.
- [39] S. Mallet. *A wavelet tour of signal processing 3rd ed.* Elsevier Inc., Burlington, MA, 2009.
- [40] R. Marques, C. Bouville, M. Ribardiere, L.P. Santos, and K. Bouatouch. Spherical Fibonacci point sets for illumination integrals. *Comput. Graph. Forum*, 32(8):134–143, 2013.
- [41] H.M. Mhashar, F.J. Narcowich, J. Prestin, and J.D. Ward. l^p Bernstein estimates and approximation by spherical basis functions. *Math. Comp.*, 79(271):1647–49, 2010.
- [42] T. Michaels. Equidistributed icosahedral configurations on \mathbb{S}^2 . in preparation.
- [43] R.D. Nair, S.J. Thomas, and R.D. Loft. A discontinuous galerkin transport scheme on the cubed sphere. *Mon. Weather Rev.*, 135:814–828, 2005.

- [44] R. Nerattini, J.S. Brauchart, and M. K.-H. Kiessling. Optimal N-point configurations on the sphere: magic numbers and Smale’s 7th problem. *J. Stat. Phys.*, 157(6):1138–1206, 2014.
- [45] H. Niederreiter. *Random number generation and quasi-Monte Carlo methods*. Soc. Ind. Appl. Math., Philadelphia, Pennsylvania, 1992.
- [46] A. Okabe, B. Boots, K. Sugihara, and S.N. Chiu. *Spatial tessellations: concepts and applications of Voronoi diagrams*. Wiley, Chichester, 1992.
- [47] E.A. Rakhmanov, E.B. Saff, and Y.M. Zhou. Minimal discrete energy on the sphere. *Math. Res. Lett.*, 1:647–662, 1994.
- [48] M. Reimer. Quadrature rules for the surface integral of the unit sphere based on extremal fundamental systems. *Math. Nachr.*, 169:235–241, 1994.
- [49] M. Reimer. Spherical polynomial approximation: a survey. In *Adv. Multivar. Approx.*, pages 231–252. Wiley, Berlin, 1999.
- [50] A. Reznikov and E.B. Saff. The covering radius of randomly distributed points on a manifold. *Internat. Math. Res. Notices*, To appear.
- [51] W.M. Schmidt. Irregularities of distribution VI. *Compos. Math.*, 24:63–74, 1972.
- [52] I.H. Sloan and R.S. Womersley. Extremal systems of points and numerical integration on the sphere. *Adv. Comput. Math.*, 21:107–125, 2004.
- [53] S. Smale. Mathematical problems for the next century. *Math. Intelligencer*, 20:7–15, Spring 1998.
- [54] J.P. Snyder. An equal-area map projection for polyhedral globes. *Cartographica*, 29(1):10–21, 1992.
- [55] J.P. Snyder. *Flattening the Earth*. University of Chicago Press, Chicago, 1993.
- [56] L. Song, A.J. Kimerling, and K. Sahr. Developing an equal area global grid by small circle subdivision. In M. Goodchild and A.J. Kimerling, editors, *Discrete global grids: a web book*. University of California, Santa Barbara, 2002.
- [57] K.B. Stolarsky. Sums of distances between points on a sphere II. *Proc. Amer. Math. Soc.*, 41:575–582, 1973.
- [58] S.L. Svensson. Finite elements on the sphere. *J. Approx. Theory*, 40:246–260, 1984.
- [59] R. Swinbank and R.J. Purser. Fibonacci grids: A novel approach to global modeling. *Roy. Meteorol. Soc.*, 132(619):1769–1793, 2006.
- [60] N.A. Teanby. An icosahedron-based method for even binning of globally distributed remote sensing data. *Comput. Geosci.*, 32:1442–1450, 2006.
- [61] M. Tegmark. An icosahedron-based method for pixelizing the celestial sphere. *Astrophys. J.*, 470:L81–L84, 1996.

- [62] J.J. Thomson. On the structure of the atom: an investigation of the stability and periods of oscillation of a number of corpuscles arranged at equal intervals around the circumference of a circle; with application of the results to the theory of atomic structure. *Philos. Mag. Ser.*, 7(39):237–265, 1904.
- [63] G. Wagner. On mean distances on the surface of the sphere (lower bounds). *Pacific J. Math.*, 144:389–398, 1990.
- [64] G. Wagner. On mean distances on the surface of the sphere II. upper bounds. *Pacific J. Math.*, 154:381–396, 1992.
- [65] T.T. Wong, W.S. Luk, and P.A. Heng. Sampling with Hammersley and Halton points. *J. Graph. Tools*, 2(2):9–24, 1997.
- [66] G. Wright. Notes/grids/meshes on the sphere. Unpublished notes.
- [67] Y.M. Zhou. *Arrangements of points on the sphere*. PhD thesis, University of South Florida, 1995.